A periplasmic protein complex supports arabinofuranosyltransferase activity and mediates intrinsic drug resistance in *Mycobacterium tuberculosis*

Thaís Klevorn[1,2], Christopher Brown[3†], Christine D. Hardy[4†], Bonnie J. Cuthbert[4†], Amanda Spencer[5], Adrián Jinich[5], Luming Chan[1], Shiva K. Angala[6], Jordan Manzer[6], Jessica Mendoza[4], Rodger de Miranda[4], Heather Kim[1], Dirk Schnappinger[1], Mary Jackson[6], Kyu Rhee[2,3], Celia W. Goulding[4,7], Sabine Ehrt[1,2]*

[1]Department of Microbiology and Immunology, Weill Cornell Medical College, New York, New York, USA

[2]Immunology and Microbial Pathogenesis Graduate Program, Weill Cornell Graduate School of Medical Sciences, Cornell University, New York, New York, USA

[3]Department of Medicine, Weill Cornell Medical College, New York, New York, USA

[4]Department of Molecular Biology & Biochemistry, University of California Irvine, Irvine, California, USA

[5]Department of Chemistry & Biochemistry, Skaggs School of Pharmacy & Pharmaceutical Sciences, University of California San Diego, San Diego, California, USA

[6]Mycobacteria Research Laboratories, Department of Microbiology, Immunology and Pathology, Colorado State University, Fort Collins, Colorado, USA.

[7]Department of Pharmaceutical Sciences, University of California Irvine, Irvine, California, USA

[†]These authors contributed equally to this work.

*Corresponding author.

Abstract

The intrinsic drug resistance of *Mycobacterium tuberculosis* (Mtb) is a major barrier to effective tuberculosis (TB) treatment, largely due to its complex, impermeable cell envelope. We identified a periplasmic protein complex comprising FecB and Rv3035 that is essential for maintaining envelope integrity and mediating intrinsic multidrug resistance in Mtb. FecB interacts with Rv3035, forming a stable heterodimer that associates with the cell envelope biosynthesis protein AftB. We

report the structures of Rv3035 alone and in complex with FecB and identify critical residues for complex formation and function. Co-essentiality and genetic interaction analyses support a functional link between FecB, Rv3035 and AftB, an arabinofuranosyltransferase which synthesizes arabinogalactan and lipoarabinomannan. Loss of FecB or Rv3035 disrupted AftB-mediated arabinan synthesis, suggesting that these proteins support AftB's enzymatic activity. Importantly, FecB is required for Mtb virulence in mice, underscoring its physiological relevance. These findings highlight FecB, Rv3035 and AftB as promising therapeutic targets.

Introduction

Tuberculosis (TB) remains the world's leading cause of death from a single infectious agent and is responsible for over 1 million deaths annually (*1*). Unlike most bacterial infections, successful TB treatment requires multiple antibiotics taken for several months, even in drug-susceptible cases. This prolonged therapy is in part due to the intrinsic drug resistance of *Mycobacterium tuberculosis* (Mtb), the causative agent of TB (*2*). A key contributor to this resistance is Mtb's complex, multi-layered cell envelope, which acts as a protective barrier against antibiotics and host immune defenses (*3*). Despite its central role in Mtb's pathogenicity and drug resistance, the molecular mechanisms governing the structure, assembly, and function of the mycobacterial cell envelope remain incompletely understood (*4*).

To identify novel targets that could potentiate existing TB therapies and shorten treatment duration, we previously performed a genome-wide chemical-genetic screen using transposon mutagenesis and sequencing (*5*). This identified *fecB* (Rv3044) as a gene whose disruption sensitized Mtb to multiple antibiotics with various mechanisms of action. These included rifampicin and ethambutol, which are part of the standard treatment regimen for drug-susceptible TB, and pretomanid, which is part of the BPaL (bedaquiline, pretomanid, linezolid) regimen used to treat drug-resistant TB (*5*). Functional studies of a Mtb *fecB* knockout strain (Δ*fecB*) revealed that *fecB* is essential for maintaining the impermeability of the Mtb cell envelope (*5*).

In Mtb, FecB is annotated as a periplasmic substrate-binding protein homologous to FecB from *Escherichia coli*, which mediates ferric citrate transport (*6*). However, Mtb lacks several canonical components of the ferric citrate transport system. Instead, Mtb FecB binds heme and the siderophore carboxymycobactin and interacts with components of the mycobacterial siderophore transport machinery (*7*). Despite these biochemical insights, the physiological role of FecB in Mtb is not fully defined. Here, we investigated how FecB contributes to Mtb's intrinsic antibiotic

resistance and uncovered a critical functional interaction with Rv3035, a previously uncharacterized periplasmic protein. Rv3035 not only interacts with FecB, but also with the arabinofuranosyltransferase AftB (Rv3805c), bridging these two proteins to form a larger complex that is important for cell envelope biogenesis.

Given the urgent need for shorter and more effective TB treatments, elucidating mechanisms that underlie Mtb's intrinsic drug resistance is of high therapeutic relevance (*2*, *3*). By characterizing the function of FecB and Rv3035 in Mtb, this study advances our understanding of periplasmic proteins in mycobacteria and highlights these proteins as promising targets for combination therapies aimed at enhancing the efficacy of existing anti-TB drugs.

Results

Mtb∆*fecB* displays a transcriptional iron deprivation signature and accumulates siderophores

Transcriptome analysis can provide functional insights by identifying pathways that are differentially regulated in a mutant strain compared to a wild type (WT) strain. These changes may reflect the mutant strain's need to adapt in the absence of the gene of interest (*8*). To gain insight into the function of FecB, we performed transcriptomic analysis by RNA sequencing of Mtb WT, ∆*fecB* and a complemented strain (∆*fecB::fecB,* containing a chromosomally integrated plasmid expressing *fecB* from the *hsp60* promoter). We decided to compare the transcriptional profile of the strains in regular growth conditions with detergent (0.05% Tween80) and without detergent, because the presence of Tween80, although helpful to prevent excessive clumping of mycobacterial cultures, also strips the mycobacterial capsule and some surface exposed lipids (*9*), making it a less physiologically relevant condition.

Compared to WT and the complemented strain, ∆*fecB* significantly upregulated the *iniBAC* operon, which is known to be induced in response to cell wall stress (*10*), both in the presence and absence of detergent in the medium (Fig. 1A and data S1). Furthermore, in detergent-free conditions, 61% of the upregulated (22 of 36) and 13% of downregulated (3 of 23) differentially expressed genes (DEGs) were related to iron utilization. The upregulated DEGs included all 14 siderophore biosynthesis genes (*mbtA-mbtN*), the genes that encode the IrtA/B transporter for siderophore uptake (*irtA*, *irtB*) and the ESX-3 secretion system substrates (*esxG*, *esxH*), which are required for mycobactin-mediated iron acquisition. The downregulated DEGs included *bfrB*,

92 encoding the iron storage protein bacterioferritin (Fig. 1, A and B). When grown in detergent-free
93 medium, Δ*fecB* thus displays a transcriptional iron deprivation signature even though the medium
94 contains a high concentration of iron. This iron deprivation signature is conditional, and it was not
95 present when Tween80 was included in the medium (Fig. 1A). One potential explanation for this
96 difference in transcriptional response is that Tween80's stripping of the capsule and some outer
97 membrane lipids might facilitate uptake of iron in Δ*fecB* during growth in regular medium.

98 Further supporting the transcriptomics data, the iron starvation signature in Δ*fecB* in detergent-
99 free medium was accompanied by an accumulation of cell-associated siderophores as identified
100 by mass-spectrometry analysis of lipid extracts (Fig. 1C). Taken together, these data suggest that
101 Δ*fecB* may be less efficient in acquiring iron in detergent-free medium due to interrupted
102 siderophore export through the periplasm, mycobacterial outer membrane and/or capsule.

103

104 **FecB is non-critical for mycobactin-mediated iron acquisition in Mtb**

105 To further probe FecB's potential role in iron acquisition, we analyzed the growth of Δ*fecB*, WT
106 and Δ*fecB*::*fecB* in iron-limiting conditions (Fig. 1D). We included a siderophore mutant,
107 MtbΔ*mbtK*, to ensure that the growth medium was iron limiting. After starving the strains for iron
108 to deplete internal iron stores and then growing them in either high or low iron conditions (iron-
109 chelated medium with 160 μM or 1 μM ammonium ferric citrate, respectively), we observed only
110 a minor growth defect of Δ*fecB* compared to the control strains, both in the presence (Fig. 1D) or
111 absence of detergent (fig. S1A). Upon passaging the strains growing in low iron into both high
112 and low iron conditions, the growth defect was still subtle and much weaker than the strong growth
113 defect of Δ*mbtK* (Fig. 1D).

114 FecB can bind to ferric- and apo-carboxymycobactin with high affinity *in vitro*, and this binding is
115 disrupted by mutating key residues E339, R240 and Y242 (*7*). To test whether binding to
116 siderophores is required for complementing Δ*fecB*'s iron-related phenotypes, we cloned and
117 expressed FecB variants harboring the mutations E339S together with R240S or Y242S in Δ*fecB*.
118 The FecB variants with significantly reduced binding affinity to ferric-carboxymycobactin
119 (E339S_R240S and E339S_Y242S) fully reversed the iron deprivation transcriptional signature
120 (examined by representative gene expression of *mbtB*, *ppe37* and *irtA*) in detergent-free medium
121 (Fig. 1E) and the subtle growth defect in low iron (fig. S1B). This complementation was particularly
122 remarkable given that the variant proteins were not clearly detectable in whole cell lysates via
123 western blot (fig. S1C). However, we note that the FecB E339S_R240S and E339S_Y242S

124 double mutants bind apo-carboxymycobactin with similar (or slightly higher) affinity than WT FecB
125 (fig. S1D). Thus, we cannot rule out that binding apo-siderophores is an important function of
126 FecB.

127 Taken together, these results suggest that FecB plays a role in iron acquisition in Mtb, however,
128 the subtle growth defect of Δ*fecB* in iron-limiting conditions points to a condition-dependent non-
129 critical function that is likely compensated for by other proteins required for iron acquisition.

130

131 **FecB's role in intrinsic multidrug resistance is distinct from its activity in iron homeostasis**

132 FecB is critical for Mtb's cell envelope impermeability and resistance to multiple antibiotics (*5*). To
133 test whether FecB's activity in iron homeostasis is related to its activity in mediating cell envelope
134 integrity and multidrug resistance in Mtb, we tested whether the FecB variants with reduced
135 binding to ferric-carboxymycobactin could rescue the antibiotic hypersusceptibility of Δ*fecB*.
136 Vancomycin and rifampicin were chosen for minimal inhibitory concentration (MIC) assays
137 because Δ*fecB* is significantly more susceptible to these drugs compared to WT(*5*).
138 Complementation of Δ*fecB* with the FecB double mutants (E339S_R240S and E339S_Y242S)
139 fully rescued Δ*fecB*'s hypersusceptibility to vancomycin and rifampicin (Fig. 2A) indicating that
140 ferric-carboxymycobactin binding is not required for FecB's function in mediating antibiotic
141 resistance.

142 To explore whether siderophore accumulation in Δ*fecB* (Fig. 1C) leads to antibiotic
143 hypersusceptibility, we interrupted siderophore biosynthesis via CRISPR interference (CRISPRi)
144 knockdown (KD) of the mycobactin biosynthesis gene *mbtI* in Δ*fecB*. If siderophore accumulation
145 is directly related to increased antibiotic susceptibility in Δ*fecB*, reducing siderophore production
146 by knocking down *mbtI* should relieve this phenotype. We validated the KD of *mbtI* in WT and
147 Δ*fecB* backgrounds by growing the strains in iron-limiting conditions, in the presence or absence
148 of anhydrotetracycline (ATc) to activate CRISPRi (fig. S2A). In the presence of ATc, the *mbtI* KD
149 strains failed to grow with ammonium ferric citrate concentrations lower than 1 μM, similarly to
150 Δ*mbtK*, indicating that siderophore production is significantly impaired through silencing of *mbtI*.
151 We next measured the MICs of vancomycin and rifampicin against the *mbtI* KD strain in the
152 presence or absence of ATc (Fig. 2B). Silencing *mbtI* with ATc did not alter the MICs, indicating
153 that siderophore accumulation is likely not the cause of antibiotic hypersusceptibility in Δ*fecB*.

154 To further test whether siderophores are involved in the antibiotic hypersusceptibility of Δ*fecB*, we
155 tested whether induction of siderophore biosynthesis would enhance Δ*fecB*'s susceptibility to
156 vancomycin and rifampicin. We performed MIC assays in low iron medium, where siderophore
157 synthesis is induced, and in regular medium, where siderophore synthesis is suppressed (Fig. 2C
158 and fig. S2B). Additionally, since an iron-starvation transcriptional signature, which includes the
159 overexpression of siderophore biosynthesis genes, was observed in Δ*fecB* only in the absence of
160 detergent (Fig. 1A), we also tested whether the mutant's antibiotic hypersusceptibility increased
161 in detergent-free medium compared to medium containing 0.05% Tween80 (fig. S2C). Contrary
162 to what would be expected if siderophores promote antibiotic hypersusceptibility, the differences
163 of the vancomycin and rifampicin MICs against Δ*fecB* compared to WT and Δ*fecB*::*fecB*
164 decreased in low iron medium compared to regular iron rich medium (Fig. 2C). Similarly, a
165 reduced shift of MICs was observed in detergent-free conditions (fig. S2C). These results do not
166 support a direct involvement of siderophores in the antibiotic hypersusceptibility phenotype of
167 Δ*fecB.* The reduced differences in antibiotic MICs might be due to slowed growth rates of the
168 strains in low iron medium and increased clumping in detergent-free medium, which hinder
169 accurate optical density measurements. In summary, these experiments dissociate FecB's role in
170 iron homeostasis from that in antibiotic resistance.

171

172 **FecB and Rv3035 interact in Mtb and likely function in the same cellular pathway**

173 FecB is classified as a periplasmic substrate-binding protein that has been shown to interact with
174 siderophore-mediated iron transport proteins (*7*). Since our data point to an alternative role for
175 FecB in mediating intrinsic drug resistance in Mtb, we set out to identify additional physical
176 interactors of FecB that could shed light on other pathways in which FecB might participate.
177 Immunoprecipitation and mass spectrometry analysis of FLAG-tagged FecB was performed and
178 analyzed in comparison to the immunoprecipitation of a WT lysate control to eliminate non-specific
179 interactions.

180 The most highly enriched interactor in our dataset was the uncharacterized protein Rv3035 (Fig.
181 3A). Rv3035 is annotated as an essential hypothetical protein containing WD40 repeats that
182 together are predicted to form an eight-bladed β-propeller structure. These domains can serve as
183 scaffolds in protein-protein interactions and the formation of multiprotein complexes and play
184 important roles in prokaryotes and eukaryotes (*11*). We confirmed binding of FecB to Rv3035 by
185 co-immunoprecipitation of the tagged proteins (fig. S3) and then set out to identify Rv3035's

186 physical interactors by using Rv3035 as the bait in a second immunoprecipitation experiment.
187 Satisfyingly, FecB was the most enriched protein in the immunoprecipitate of Rv3035-3xFLAG,
188 compared to the WT lysate control (Fig. 3B). In addition, AftB and Rv0227c, which are the other
189 two most enriched interacting partners of FecB, were also among the most enriched partners of
190 Rv3035 (Fig. 3, A and B, and data S2).

191 To further inform our proteomics findings, we investigated the genetic interactions of *fecB* via co-
192 essentiality/co-fitness analysis. This method allows the detection of gene pairs that share similar
193 fitness profiles across forward genetic screens, and thus can help identify genes that encode
194 proteins with similar or related function (*12*). Using a publicly available CRISPRi chemical-genetic
195 interaction dataset which profiled gene essentiality across 80 drug-treatment and CRISPRi pre-
196 depletion conditions (*13*), we performed co-essentiality analysis using generalized least squares
197 (GLS) regression of *fecB*, *rv3035*, and the genes encoding their most enriched common protein
198 interactors, *aftB* and *rv0227c*. While *rv0227c* did not share an essentiality profile with the others,
199 *fecB*, *rv3035* and *aftB* were all hits in each other's co-essential gene clusters (Fig. 3, C and D).
200 This analysis identified 13 genes co-essential with *fecB*, 19 with *rv3035* and 22 with *aftB*, among
201 which 4 were shared by all three (Fig. 3D and data S3).

202

203 **FecB forms a complex with Rv3035 *in vitro***

204 To confirm the direct binding of Rv3035 and FecB *in vitro*, we cloned His-tagged Rv3035 from
205 *Mycobacterium thermoresistible* (Mth). Mth Rv3035 shares 67% sequence identity with Mtb
206 Rv3035 (fig. S4A) and was used because full-length or N-terminal truncation constructs of His-
207 tagged Mtb Rv3035 failed to yield soluble protein. Mth Rv3035 is predicted to have an N-terminal
208 signal peptide by SignalP 6.0 (*14*) and to be a lipoprotein, where the N-terminal cysteine residue
209 is predicted to form a thioether linkage to diacylglycerol (*15*, *16*). Here, we have designated this
210 N-terminal cysteine as the first amino acid of the mature form of Rv3035 (fig. S4B). Our Mth
211 Rv3035 protein construct begins at residue 2 of the predicted mature protein and was expressed
212 with a cleavable, N-terminal His-tag. Mth Rv3035-His was purified to homogeneity and the His-
213 tag cleaved, with size-exclusion chromatography (SEC) of the resulting protein suggesting that
214 Mth Rv3035 is monomeric (fig. S5A).

215 Mth Rv3035-His was also co-expressed with untagged Mtb FecB and found to co-elute by Ni-
216 affinity chromatography (fig. S5B). The Mth Rv3035 and Mtb FecB complex was stable during
217 SEC and displayed a molecular weight of 79.1 kDa, consistent with a heterodimer of Rv3035 and

218 FecB (fig. S5A). The affinity of Mth Rv3035 for Mtb FecB was quantified using isothermal titration
219 calorimetry (ITC). This analysis revealed tight 1:1 binding of Mth Rv3035 and Mtb FecB, with a
220 K_D of 27.5 ± 4.6 nM (Fig. 4A).

221

222 **Structure determination of Rv3035 and the FecB-Rv3035 complex**

223 We next solved the structure of Mth Rv3035 by X-ray crystallography to 1.9 Å (table S1). Mth
224 Rv3035 crystallized with two subunits in the asymmetric unit. In both subunits, there is clear
225 electron density for all but the N-terminal seven residues of Rv3035. The two subunits are virtually
226 identical with a root mean square deviation (rmsd) of 0.46 Å over 392 residues.

227 The structure of Rv3035 adopts a β-propeller fold, composed of eight 4-stranded β-sheets, where
228 each β-sheet is referred to as a blade (Fig. 4B and fig. S4A). At the N-terminus of the protein,
229 preceding the β-propeller fold, are ~40 residues that form an ordered loop region, which occupies
230 the bottom half of the central cavity formed by the β-propeller. A small portion of this N-terminal
231 region forms a β-strand (β_0, residues 27-32) that forms a β-sheet with the interior β-strand (β26)
232 of blade H (Fig. 4B and fig. S4A). The top half of the cavity is occupied by a second ordered loop
233 region formed by residues 171-197 containing a small α-helix (fig. S4A), which appears to act as
234 a cap (α-cap) for the central pore (Fig. 4B).

235 Mth Rv3035 contains two disulfide bonds (Fig. 4B, fig. S4A, and fig. S6A). The first is formed
236 between C71 and C87 and connects the exterior β-strand (β5) of blade B to the loop region on
237 the α-cap side of the β-propeller, and the second is formed between C187 and C194 connecting
238 the α-cap to the ordered loop region following it, perhaps stabilizing the cap region. A structural
239 homology search of Mth Rv3035 utilizing the DALI server (*17*) (table S2) demonstrated that the
240 closest hits have extremely high structural homology with Rv3035 and the majority are accessory
241 proteins that assist in remodeling protein assemblies; for example, two of the top hits are BamB
242 from Gram-negative bacteria.

243 To determine the protein-protein interacting residues of the FecB-Rv3035 complex, we solved the
244 X-ray crystal structure of the FecB-Rv3035 complex to a resolution of 3.35 Å (table S1). There
245 are minimal structural differences between FecB alone (*7*) and FecB in complex with Rv3035 (fig.
246 S6, C and D). One notable difference is the presence of a disulfide bond between C56 and C104
247 (fig. S6D), which is absent in the previous FecB crystal structure. Likewise, there are little
248 differences between the structures of Rv3035 alone and in complex with FecB (fig. S6, E and F).

249 The FecB-Rv3035 complex interface is small and involves 729 $Å^2$ (5.6%) of the FecB surface,
250 and 692 $Å^2$ (4.3%) of Rv3035 (Fig. 4C). Although the interface is small, there are multiple
251 interactions between the two proteins including 19 hydrogen bonds and salt bridges that are $\leq$
252 3.5 Å and six interactions that are < 3.0 Å (Fig. 4D and table S3). The interface involves residues
253 from Rv3035 blade B (β4-β5) and residues from the loop that precedes blade B (between β1 and
254 β2) (Fig. 4D and fig. S4A). The interface also involves the backbone nitrogen atom from disulfide
255 bond forming C71 (Fig. 4D and fig. S6B). Strikingly, only nine Rv3035 residues are responsible
256 for the polar interactions at the interface, with six residues forming multiple contacts with FecB:
257 R43, K46, E77, R83, Q84, and R85, where R83 forms four polar contacts at the interface. FecB
258 residues participating in the polar contacts at the interface are localized to the second lobe of
259 FecB and are located in α7 (D223, H226), the loop between α8 and α9 (D258), the loop between
260 α10B and β11 (A291, D292), and α13 (S320, R323, D324)(*7*). Similar to Rv3035, several FecB
261 residues are responsible for multiple contacts at the interface: H226, D292, S320, R323 and
262 D324; where D292 forms five and D324 forms four polar contacts at the interface. The FecB-
263 Rv3035 interface leaves the ligand binding site of FecB accessible to solvent, and thus still able
264 to accommodate a ligand (Fig. 4C).

265

266 **Key FecB residues for binding Rv3035**

267 To test the functional importance of FecB residues involved in binding Rv3035, we mutated FecB
268 D292 to alanine alone or H226, D292 and D324 to alanine together, and tested binding of these
269 proteins to Rv3035 by protein interaction pull-down assays and by ITC. After determining that the
270 mutants were properly folded by circular dichroism (fig. S7A), we utilized FecB-His and untagged
271 Rv3035 in a nickel-affinity pull-down assay (fig. S7B). While WT FecB-His copurified with Rv3035,
272 FecB D292A alone and the FecB triple mutant H226A_D292A_D324A failed to pull down Rv3035.
273 In addition, binding to Rv3035 was not observed for the single and triple FecB mutants by ITC
274 analysis (fig. S7C). Thus, the nanomolar affinity (K_D of ~30 nM) interaction between FecB and
275 Rv3035 can be completely disrupted by mutating one FecB residue, D292.

276

277 **Rv3035 mediates intrinsic multidrug resistance in Mtb**

278 Having demonstrated that FecB and Rv3035 interact both *in vivo* and *in vitro*, we next set out to
279 probe the cellular function of Rv3035. In TnSeq screens, *rv3035* mutants are usually annotated

280 as having a “growth defect” (*18*) and are often absent from TnSeq screen input libraries. That is
281 likely the reason why *rv3035* was not a hit in our TnSeq chemical-genetic interaction screen that
282 identified *fecB* as important for intrinsic antibiotic resistance in Mtb (*5*). Because *fecB* and *rv3035*
283 display similar growth defects by CRISPRi (*19*), we reasoned that it would be possible to generate
284 a *rv3035* knockout strain (Δ*rv3035*) to test directly whether Rv3035 mediates intrinsic resistance
285 to different antibiotics. Although Δ*rv3035* colonies took longer to grow on agar plates than WT
286 Mtb, the mutant strain exhibited similar growth kinetics as WT and Δ*fecB* in liquid media (fig. S8A).
287 Additionally, we generated a Δ*fecB* Δ*rv3035* double knockout as well as the respective
288 complemented mutants.

289 We performed MIC assays using these strains for several antibiotics having different mechanisms
290 of action to which Δ*fecB* was hypersusceptible (Fig. 5A). Isoniazid was included as a control
291 because its MIC is not affected by the absence of *fecB* (*5*). The single Δ*rv3035* and double
292 Δ*fecB*Δ*rv3035* mutants showed very similar antibiotic hypersusceptibility patterns as Δ*fecB*, with
293 reduced MICs compared to WT. As the basis for Δ*fecB*’s hypersusceptibility to antibiotics is likely
294 a more permeable cell envelope compared to WT Mtb (*5*), we also tested whether Δ*rv3035* and
295 Δ*fecB*Δ*rv3035* are more permeable to fluorescently labelled vancomycin and the reporter dye
296 calcein-AM (*20*). Both mutants phenocopied Δ*fecB* with increased uptake of BODIPY-vancomycin
297 (Fig. 5B) and both were hyperpermeable to calcein-AM similarly to Δ*fecB* (Fig. 5C).

298 Δ*fecB* also displayed altered colony morphology and a growth defect when growing as single
299 colonies on agar plates, appearing smooth on high density spots and often failing to grow in lower
300 spot dilutions (Fig. 5D). This makes experiments that rely on the quantification of Δ*fecB* colony
301 forming unit (CFU) titers unreliable. Although we do not know the basis of this phenotype, it could
302 be related to cell envelope alterations. Δ*rv3035* and Δ*fecB*Δ*rv3035* displayed the same defect
303 (Fig. 5D). Taken together, these results demonstrate that Rv3035 is important for intrinsic
304 multidrug resistance, mediates cell envelope impermeability and is required for regular growth on
305 solid media. Importantly, deleting *fecB* and *rv3035* in the same strain did not result in enhanced
306 phenotypes (Fig. 5, A-D), a result that it is expected for genes functioning in the same pathway.

307 To test whether binding between FecB and Rv3035 is required for maintaining cell envelope
308 integrity, we complemented Δ*fecB* with an integrated plasmid expressing the FecB triple mutant
309 H226A_D292A_D324A which fails to bind Rv3035 *in vitro* (fig. S7C). First, we confirmed that the
310 FecB triple mutant is stably expressed *in vivo* (fig. S8B). Then, we tested whether Δ*fecB*
311 complemented with the triple mutant (Δ*fecB*::*fecB*-H226A_D292A_D324A) can rescue Δ*fecB*’s
312 hypersusceptibility to vancomycin and rifampicin. The MICs of these drugs were unchanged in

313 Δ*fecB*::*fecB*-H226A_D292A_D324A compared to Δ*fecB* (Fig. 5E). Similarly, the FecB triple mutant
314 failed to rescue Δ*fecB*'s growth defect in solid media (fig. S8C). These results indicate that FecB's
315 binding to Rv3035 is critical to mediate intrinsic drug resistance in Mtb.

316

317 **FecB and Rv3035 interact with cell envelope biosynthesis proteins**

318 Our immunoprecipitation data revealed that FecB and Rv3035 also interact with the cell envelope
319 biosynthesis proteins AftB and Rv0227c (Fig. 3, A and B), which was confirmed by co-
320 immunoprecipitation assays (fig. S9 and S10). Moreover, *fecB* and *rv3035* are co-essential with
321 *aftB* (Fig. 3C), which suggests they may perform similar functions and could be part of a protein
322 complex (*12*). AftB catalyzes the last step in the biosynthesis of the arabinan domain of
323 arabinogalactan (AG) and lipoarabinomannan (LAM), adding the terminal β-arabinofuranose (β-
324 Ara*f*) residue to those molecules (*21*). In AG, the terminal β-Ara*f* and the penultimate α2-linked
325 Ara*f* residue provide mycolic acid (MA) attachment sites which are critical for the formation of the
326 mycolyl–arabinogalactan–peptidoglycan (mAGP) complex (*22*, *23*). Rv0227c (named polar
327 growth factor A, or PgfA, in *Mycobacterium smegmatis*) is an inner membrane protein that
328 interacts with MmpL3, the transporter for the cell envelope component trehalose monomycolate
329 (TMM), and with a TMM analog, suggesting that it participates in TMM transport across the
330 plasma membrane (*24*).

331 In the periplasm, TMMs may donate a mycoloyl residue to AG to form the mAGP complex or to
332 another TMM molecule to form trehalose dimycolate (TDM or cord factor) (*25*). While MAs
333 attached to AG (mAG) are the major components of the inner leaflet of the mycobacterial outer
334 membrane (MOM), TMMs, TDMs and free MAs are thought to populate both the outer and inner
335 leaflets of the MOM (*3*). These lipids are critical determinants of Mtb's cell envelope
336 impermeability (*3*). Since AftB and Rv0227c are involved in the biosynthesis of mAG and the
337 MOM, the interaction of FecB and Rv3035 with these proteins suggests that they participate in
338 the assembly or maintenance of mAG and/or the MOM.

339 We used AlphaFold 3 (*26*) to predict the potential protein complexes formed by FecB, Rv3035,
340 AftB and/or Rv0227c, modeling different combinations of these proteins (fig. S11 and S12). The
341 FecB and Rv3035 complex showed a very high per-residue model confidence score (plDDT, fig.
342 S11), and has the same interface and orientation observed in the experimental structure of FecB-
343 Rv3035, superimposing with a rmsd of 0.91 Å over 696 residues (Fig. 4C). The complexes
344 containing AftB (with or without Rv0227c) showed a higher confidence score when modeled with

Rv3035 than with FecB alone (fig. S12, B and C). These structural models crossed the interface predicted template modeling (ipTM) score threshold for high-quality prediction of 0.8 when AftB was modeled with FecB and Rv3035, with Rv3035 and Rv0227c, or when all 4 proteins were modeled together (fig. S12). This suggests that Rv3035 bridges the interaction between FecB and AftB, and between FecB and Rv0227c.

***AftB* is more vulnerable to knockdown in Δ*fecB* than in WT**

Because *aftB* shares an essentiality profile with *fecB* and *rv3035* (Fig. 3C), we decided to further explore the genetic interaction between *fecB* and *aftB.* We depleted *aftB* with a weak CRISPRi single guide RNA in both WT and Δ*fecB*. While this weak guide caused a slight growth defect in WT upon induction of the CRISPRi system, knockdown of *aftB* by the same weak guide in Δ*fecB* completely abrogated growth (Fig. 6A). This indicates that *aftB* is more vulnerable to knockdown in Δ*fecB* than in WT as a moderate depletion of *aftB* leads to a profound loss of fitness in the absence of *fecB*.

FecB, Rv3035 and AftB are required to maintain normal TMM levels in Mtb

To test whether FecB is required for proper assembly of the MOM, we performed lipidomics analysis of total extractable lipids from WT, Δ*fecB* and Δ*fecB*::*fecB* strains (Fig. 6, B and C, and data S4). Contrary to expectations that mycolate levels would be reduced in Δ*fecB* due to their role in mediating envelope impermeability, the mutant displayed a higher abundance of TMMs and free MAs compared to WT and Δ*fecB*::*fecB*.

Since TMMs accumulate in the plasma membrane of TMM transport mutants (*24*, *27–29*), we next assessed if lipid trafficking was disrupted in Δ*fecB*. We treated bacterial pellets with the anionic surfactant dioctylsulfosuccinate sodium (AOT) dissolved in heptane to strip non-covalently bound lipids off the MOM (*30*). In *Corynebacterium glutamicum*, AOT in heptane forms reverse micelles which solubilize and capture OM surface lipids but does not penetrate other layers of the cell envelope (*30*). We validated this approach by analyzing known lipids extracted from the supernatants and pellets of AOT treated samples, corresponding to the outer leaflet of the MOM (labelled OM) and all other extractable lipids (labeled inner membrane or IM), respectively (fig. S13, A-D, and data S4). Δ*fecB* displayed a higher abundance of TMMs and free MAs in both IM and OM fractions, compared to WT and Δ*fecB*::*fecB* (fig. S13, E-H, and data S4). We used the

376 OM fraction to visualize and quantify TDMs via thin-layer chromatography (Fig. 6D and fig. S13I).
377 Although TDM levels are inversely correlated with TMMs in mutants with defective TMM transport
378 (*24*, *27–29*), Δ*fecB* also displayed increased TDM levels compared to controls.

379 To validate the lipidomics data with an alternative method, we used the solvatochromic trehalose
380 probe DMN-Tre to track MA incorporation into TMMs via flow cytometry (*31*). Upon entering the
381 cell, DMN-Tre is mycolylated to form DMN-Tre monomycolates, which are subsequently inserted
382 into the MOM, where the hydrophobic environment activates the probe's fluorescence (*31*).
383 Corroborating the lipid analysis, Δ*fecB* incorporated more DMN-Tre in its cell envelope than WT,
384 shown as increased mean fluorescence intensity compared to WT and Δ*fecB*::*fecB* (Fig. 6E). The
385 same phenotype was observed in *aftB* KD strains upon CRISPRi activation (Fig. 6F) and in
386 Δ*rv3035* compared to controls (Fig. 6G). These results indicate that *fecB*, *rv3035* and *aftB* mutants
387 accumulate trehalose monomycolates in the MOM.

388 Overall, these data suggest that FecB, Rv3035 and AftB are important for proper assembly and/or
389 maintenance of free mycolates in the MOM.

390

391 **FecB and Rv3035 are important for arabinofuranosyltransferase function in Mtb**

392 To investigate whether the FecB-Rv3035 complex influences AftB's arabinofuranosyltransferase
393 activity, we quantified per-*O*-methylated alditol acetates derived from the mAGP complex and
394 lipoglycans (LAM and LM mixture) from WT, Δ*fecB*, Δ*rv3035* and complemented strains. 2-linked
395 arabinofuranosyl (Ara*f*) residues in the mAGP and LAM were reduced in Δ*fecB* and Δ*rv3035*,
396 compared to WT (Fig. 6, H and I). This defect was fully reversed in the mAGP and partially
397 reversed in the LAM of the complemented strains (Fig. 6, H and I). These findings are consistent
398 with reduced AftB activity in Δ*fecB* and Δ*rv3035* (*21*, *32*). The greater decrease in 2-Ara*f* linkage
399 levels in LAM (1.6-fold) compared to AG (1.2 and 1.3-fold) of the two mutants, and the more
400 efficient restoration of these glycosyl linkages in AG upon genetic complementation, indicate that
401 the available AtfB activity in each strain prioritizes the completion of the arabinan domain of AG
402 (which is critical to the formation of the MOM) over that of LAM.

403 Noticeably, in mAGP (fig. S14, A-H) the decrease in 2-Ara*f* linkages in the mAGP of Δ*fecB* and
404 Δ*rv3035* was accompanied by a modest decrease in 5-Ara*f* linkages and a reduction in overall
405 Ara*f*/Gal*f* ratio in Δ*rv3035,* suggestive of a smaller size arabinan domain compared to WT and
406 Δ*rv3035*::*rv3035* strains (fig. S14, B and H). With regards to LAM (fig. S14, I-O), the decrease in

407 2-Ara*f* linkages in Δ*fecB* and Δ*rv3035* was accompanied by a decrease in branched 3,5-Ara*f*
408 linkages and *t*-Ara*f* (fig. S14, I and K) and minor changes in the mannan domain of the lipoglycans
409 (fig. S14, L-O), except for a marked increase in 6-mannopyranosyl (6-Man*p*) residues in Δ*fecB*
410 compared to WT, and in 2,6-Man*p* and 2-Man*p* residues in Δ*rv3035* compared to WT and
411 Δ*rv3035*::*rv3035*, typifying a more branched mannan domain in LM and/or LAM (fig. S14, M-O).
412 Collectively, these structural alterations in the AG and lipoglycans of Δ*fecB* and Δ*rv3035* point to
413 greater alterations in the biosynthetic machinery of these two glycans than a sole reduction in
414 AftB activity and suggest that other arabinosyltransferases and mannosyltransferases may be
415 negatively impacted by the loss of FecB or Rv3035.

416

417 **FecB is essential for virulence of Mtb in mice**

418 The mycobacterial cell envelope is a formidable barrier that protects Mtb not only from antibiotics
419 but also from host immune responses (*3*). Thus, we hypothesized that *fecB* might also be required
420 for Mtb to establish a successful infection in mice. The unreliability of Δ*fecB* to grow as single
421 colonies on agar plates (Fig. 5D), however, impairs the quantification of the bacterial burden in
422 infected mice. To circumvent this problem, we implemented a genetic switch to activate *fecB*'s
423 expression in the presence of a tetracycline inducer (TetON) (*33*) and allow quantification of CFUs
424 from mice infected with Δ*fecB* harboring the TetON switch (FecB-TetON). The conditional
425 expression of *fecB* was validated via MIC assays with vancomycin and rifampicin, which showed
426 that addition of ATc rescued the antibiotic hypersusceptibility of FecB-TetON (Fig. 7A).

427 Mice were infected via the aerosol route with FecB-TetON and received either regular or
428 doxycycline (doxy) chow throughout the course of the experiment (Fig. 7, B and C), with doxy
429 chow inducing *fecB* expression. Lung and spleen homogenates from both groups were cultured
430 on agar containing ATc to activate *fecB* expression *ex vivo*. FecB-TetON grew and established a
431 high titer chronic infection in the lungs of mice fed with doxy-containing chow (Fig. 7B). In contrast,
432 in mice receiving regular chow, in which expression of *fecB* is silenced, FecB-TetON grew during
433 the first 14 days post-infection (p.i.), after which CFU counts remained relatively stable for another
434 8 weeks p.i. Dissemination to the spleen was delayed, and similarly to the lung, spleen bacterial
435 burden was significantly lower in mice receiving regular versus doxy chow (Fig. 7C). Thus, we
436 conclude that *fecB* is required for Mtb virulence and plays a critical role during growth in the acute
437 phase of infection but is not required for Mtb's persistence in the host.

438

Discussion

The mycobacterial cell wall, comprised of peptidoglycan, arabinogalactan and mycolic acids, has been a key target of several anti-TB drugs (*34*). Two of the four first-line TB drugs, isoniazid and ethambutol, target mycolic acid and arabinogalactan biosynthesis, for instance. Although these drugs were developed more than 60 years ago, they remain part of the standard TB chemotherapy due to their success in treating drug-susceptible Mtb infections, which validates efforts to explore novel inhibitors that target the cell wall of Mtb (*10*). Despite being an important target for drug development and playing a central role in Mtb pathogenesis and intrinsic drug resistance, many aspects of the Mtb cell wall, and more broadly, cell envelope, such as factors involved in their assembly and maintenance remain unknown. In the current study, we describe two periplasmic proteins, FecB and Rv3035, that work together to support arabinofuranosyltransferase activity, mediate cell envelope impermeability and impart intrinsic multidrug resistance in Mtb.

Our transcriptomic data indicate that Mtb lacking *fecB* upregulates the *iniBAC* operon (**i**so**n**iazid **i**nduced genes B, A and C), which is named for being induced by isoniazid, ethambutol, and other inhibitors of cell wall biosynthesis (*10*). Upregulation of the *iniBAC* genes in Δ*fecB* occurred independently of the presence of detergent in the media and most likely reflects a constitutive defect in cell wall integrity, which results in Δ*fecB's* increased membrane permeability (*5*).

The iron deprivation transcriptional signature and accumulation of siderophores in Δ*fecB* grown in detergent-free media points to *fecB* having an activity in iron homeostasis. However, whether this is a direct or indirect effect remains unclear. While FecB can bind ferric-carboxymycobactin with high affinity *in vitro* (*7*), experiments probing the requirement of *fecB* for iron acquisition *in vivo* showed only minor growth phenotypes. FecB variants with lower binding affinity to ferric-carboxymycobactin (FecB E339S_R240S and E339S_Y242S) rescued the iron deprivation transcriptional signature and slower growth of Δ*fecB* in iron-limiting conditions, suggesting that binding to iron-loaded siderophores is dispensable in FecB's ability to reverse these phenotypes. On the other hand, FecB E339S_R240S and E339S_Y242S have slightly higher binding affinity to apo-carboxymycobactin and thus we could not test the *in vivo* requirement of FecB's binding to iron-free apo-siderophores using these variants. Importantly, using FecB E339S_R240S and E339S_Y242S, and other genetic and microbiological approaches, we showed that FecB's role in iron homeostasis is likely not connected to its role in mediating antibiotic resistance in Mtb.

Specific evidence for FecB's function in cell envelope integrity came to light upon identification of FecB's most enriched physical interactors: Rv3035, AftB and Rv0227c. In *Mycobacterium*

471 *marinum*, FecB was also found to interact with AftB and the Rv3035 homologue MMAR_1667
472 (*35*). Although AftB's function has been well described in the literature (*21*, *32*, *36*), only a few
473 studies explore the function of Rv0227c (*24*, *37*) and Rv3035 (*35*) homologues in mycobacteria.
474 Here we report on the structure of Rv3035 alone and of the FecB-Rv3035 complex, which
475 identified key FecB residues involved in binding Rv3035 that we were able to validate
476 experimentally. Moreover, we show that FecB's binding to Rv3035 is required for its function in
477 mediating antibiotic resistance in Mtb. Mtb∆*rv3035* and the double knockout ∆*fecB*∆*rv3035*
478 displayed the same phenotypes indicative of perturbed cell envelope integrity as ∆*fecB*. This
479 indicates that the absence of either protein equally impacts the function of the complex and thus
480 both are required to fulfill their function.

481 Structural homology analysis for Rv3035 revealed two classifications of structural homologs (table
482 S2). One class represents assembly factors that contribute to scaffolding in larger complexes,
483 facilitating the coordinated movement of multiple protein components. This includes BamB of the
484 prokaryotic β-barrel assembly machinery (BAM) complex, and the eukaryotic ODA16, an
485 assembly factor involved in outer dynein arm intraflagellar transport (*38*). When comparing these
486 structural homologs to Rv3035, both the N-terminal propeller cavity plug region and the α-cap
487 present in Rv3035 are absent in these assembly factors. The second class of Rv3035 structural
488 homologs have enzymatic activity. Strikingly, these structural homologs - *Acidithiobacillus*
489 *ferrooxidans* tetrathionate hydrolase (*39*), *Methylacidiphilum fumariolicum* SolV methanol
490 dehydrogenase (*40*), and the *Devosia albogilva* quinone-dependent dehydrogenase (*41*) - all
491 have secondary structure elements similar to the Rv3035 α-cap and bear an N-terminal propeller
492 central cavity plug. However, in these enzymatic structural homologs, the propeller fold is more
493 extensively decorated than in Rv3035. Indeed, Rv3035—due to the presence of the N-terminal
494 propeller cavity plug and the propeller decorations—has greater similarity with its enzymatic
495 structural homologs than it does with the assembly factor homologs. Although our studies show
496 that Rv3035 acts as a scaffolding protein in its interactions with FecB, its resemblance to the
497 enzymatic homologs raises the possibility that Rv3035 may possess an as-yet unidentified
498 enzymatic activity.

499 What is the function of FecB and Rv3035, and how do these proteins contribute to intrinsic
500 multidrug resistance in Mtb? Our findings suggest that FecB and Rv3035 interact with AftB, a
501 known arabinofuranosyltransferase, and together form a functional complex that supports cell
502 envelope biosynthesis. Proteomic data, CRISPRi essentiality profiles, and high-confidence
503 structural predictions from AlphaFold 3 collectively support the interaction of FecB-Rv3035 with

504 AftB. In the predicted model, Rv3035 acts as a bridge between FecB and AftB, positioning the
505 periplasmic proteins in close proximity to AftB's active site cavity (*42*). The proposed orientation
506 suggests that the FecB-Rv3035 complex may serve as scaffold for AftB's engagement with its
507 substrate AG/LAM or may regulate AftB's enzymatic activity.

508 Lipidomics data further support FecB's role in AftB function as Δ*fecB* exhibited increased levels
509 of TMMs, TDMs and free MAs compared to controls. This phenotype is observed in *M. smegmatis*
510 treated with ethambutol (*43*) (inhibitor of AG/LAM biosynthesis), and in deletion mutants of *aftB*
511 (*21*) and *aftC* (*44*) (another arabinofuranosyltransferase) in *C. glutamicum* and *M. smegmatis*,
512 respectively, all of which show increased levels of trehalose mycolates. Notably, *fecB*, *rv3035* and
513 *aftB* mutants all displayed enhanced incorporation of TMMs into the MOM, a phenotype
514 exacerbated by selective depletion of *aftB* in the Δ*fecB* background. This depletion completely
515 inhibited growth in Δ*fecB*, while only mildly affecting WT, indicating that Mtb becomes more reliant
516 on full *aftB* expression in the absence of FecB.

517 Further evidence of FecB and Rv3035's functional support of AftB comes from glycosyl linkage
518 analysis. Mtb mutants lacking *fecB* or *rv3035* showed reduced levels of 2-linked Ara*f* residues in
519 AG and LAM, consistent with impaired terminal Ara*f* addition by AftB (*21*, *32*). A decreased ratio
520 of arabinose to galactose in AG was also observed in a *M. marinum fecB* mutant (*35*), supporting
521 our findings of additional alterations in length and branching of AG and LAM. Besides the impact
522 on mycolate levels and their localization, structural alterations in AG and LAM may compromise
523 overall cell envelope integrity and influence host-pathogen interactions (*32*, *35*, *45*).

524 Taken together, our data support a model in which the FecB-Rv3035 complex is essential for
525 optimal AftB activity *in vivo*. This complex contributes to the biosynthesis and structural integrity
526 of the mycobacterial cell envelope, thereby playing a key role in Mtb's intrinsic resistance to
527 antibiotics. This new understanding of the molecular mechanisms that govern Mtb's cell envelope
528 impermeability and intrinsic antibiotic resistance provides valuable insights for TB drug discovery
529 and the development of more effective regimens that may shorten TB treatment.

530

531 **Materials and Methods**

532

533 **Bacterial strains and culture conditions**

534 Mtb strains used in this study are listed in data S5. For most experiments, the strains were cultured
535 in Middlebrook 7H9 medium (BD, #271310) supplemented with 0.2% glycerol, 0.5% bovine serum
536 albumin fraction V, 0.2% dextrose, 0.085% NaCl and 0.05% Tween80 (Sigma, # P8074), this is
537 referred to as “regular” medium. For detergent-free conditions, Tween80 was omitted from the
538 media recipe. For growth in iron-limiting conditions, self-made 7H9 medium without ammonium
539 ferric citrate (AFC) was prepared and chelated for 2 days with 20g/liter of BioRad Chelex 100
540 resin. After filter-sterilization, metals other than iron were added according to their concentrations
541 in Middlebrook 7H9. To prepare Low/High Iron media, 1μM or 160μM of AFC was added to iron-
542 chelated medium, respectively. For reference, Middlebrook 7H9 medium contains 150μM AFC.
543 Where required, antibiotics or small molecules were used at the following concentrations:
544 hygromycin (50μg·ml^{-1}), kanamycin (25μg·ml^{-1}), zeocin (25μg·ml^{-1}), streptomycin (25μg·ml^{-1}),
545 apramycin (60μg·ml^{-1}) and ATc (200ng·ml^{-1} for CRISPRi strains and 1000ng·ml^{-1} for FecB-
546 TetON). The strains were grown at 37°C and 5% CO_2 in a standing incubator, unless otherwise
547 indicated.

548

549 **Plasmids construction**

550 Plasmids used in Mtb strains are listed under the strain “full name” after the double colon in data
551 S5. Plasmids starting with pGM were constructed using Invitrogen Gateway Cloning system.
552 Constructs harboring the gene of interest were synthesized by GenScript. CRISPRi constructs
553 were generated as previously described (*19*).

554

555 **RNA extraction**

556 Total RNA was extracted from 10mL of mid-log phase bacterial cultures by first adding 1:1
557 guanidinium thiocyanate buffer followed by centrifugation for 10 minutes at 4°C. Bacterial pellets
558 were bead-beaten into 0.9mL Trizol, 0.2mL chloroform was added to each sample and RNA in the
559 aqueous phase was purified using the RNA Clean and Concentrator-25 kit (Zymo Research
560 #R1017). After elution, samples were incubated with TURBO DNase (Ambion, AM2238) at 37°C
561 for 1h to remove residual genomic DNA. Samples were then repurified using the RNA Clean and
562 Concentrator-25 kit or RNA Clean and Concentrator-5 kit (Zymo Research #R1015).

563

564 **RNA-sequencing (RNA-seq) and analysis**

565 Ribosomal RNA (rRNA) was removed from total RNA as previously described (*46*). The resulting
566 rRNA-depleted RNA was then concentrated with the RNA Clean and Concentrator-5 kit (Zymo
567 Research #R1015). RNA-seq libraries were created from these samples using the NEBNext Ultra
568 II Directional RNA Library Prep Kit for Illumina (New England Biolabs, E7760L) along with
569 NEBNext Multiplex Oligos for indexing (New England Biolabs). The libraries were purified using
570 Dynabeads MyOne Streptavidin C1 (Thermo Fisher #65002), assessed for quality with a
571 Bioanalyzer, and pooled based on their unique indexes. Sequencing was carried out on an
572 Illumina NextSeq2000 platform at the Genomics Resources Core Facility of Weill Cornell
573 Medicine.

574 RNA-seq data analysis was conducted using R. Sequencing reads underwent trimming and
575 filtering with Rfastp, followed by alignment to the H37Rv reference genome (GenBank
576 AL123456.3; RefSeq NC_000962.3; GCF_000195955.2; Genome assembly ASM19595v2) using
577 the Rsubread package (*47*, *48*). BAM alignment files were generated, sorted, and indexed using
578 Rsamtools. Read quantification was carried out with featureCounts, and differential gene
579 expression analysis was performed using DESeq2 (*49*, *50*).

580

581 **Lipid extraction**

582 Mtb cultures were grown in detergent-free 7H9 containing fatty acid-free BSA until mid-log phase.
583 Bacterial pellets were transferred to sterile filters (*51*) which were added directly to 16 x 100mm
584 glass tubes containing 2:1 chloroform: methanol or to 2mL screw cap tubes containing 1mL of
585 10mM AOT dissolved in heptane or PBS as a control. For AOT treatment, pellets in AOT or PBS
586 were agitated in a bead-beater at low speed (2800rpm) for 10s to knock the cells off the filters
587 followed by removal of filters and incubation in a cooling rack for 1h, with mixing by inversion of
588 the tubes every 5 minutes. 500µL of AOT supernatant was added to 16 x 100mm glass tubes
589 containing 2:1 chloroform: methanol. AOT and PBS pellets were resuspended in 600µL of 2:1
590 chloroform: methanol and added to 16 x 100mm glass tubes containing 2:1 chloroform: methanol.

591

592 **Liquid chromatography-mass spectrometry (LC-MS) analysis**

593 Lipid extracts were centrifuged at 4000rpm for 15 minutes at 4°C and the supernatant decanted
594 into new 16 x 100mm borosilicate tubes. The tubes were dried using a GeneVac evaporator under
595 vacuum with gentle heating to 40°C. The residual residue was transferred to pre-weighed 4mL

596 amber vials using 2mL 1:1 chloroform: methanol. The solution was again dried using the GeneVac
597 evaporator. The vials were re-weighed to obtain the dry weight of lipid extract, and this mass was
598 used to prepare a 1mg/mL solution in 1:1 chloroform: methanol. Lipids were stored at -20°C as a
599 stock solution. A 150µL aliquot of stock solution was transferred to a glass insert tube (250µL,
600 Agilent Technologies) nested within a microfuge tube. The aliquot was evaporated to dryness
601 using an argon air stream then resuspended in 150µL of a solution of 70% hexanes and 30%
602 isopropyl alcohol. After briefly vortexing to resuspend, the samples were centrifuged at 4000rpm
603 for 15 minutes at 4°C. A volume of 100µL of the supernatant was transferred to a 2mL amber vial
604 (Agilent) equipped with 250µL glass insert tubes and capped with 9mm septum-embedded screw
605 caps (Agilent). A 10µL injection of this sample was analyzed using liquid chromatography mass
606 spectrometry (LC-MS) on an Agilent 6520 ESI-QTOF. Separation of lipids using a 3µm diol column
607 (2.1 x 150mm) and gradient elution from solvent A (70% hexane, 30% isopropanol, .02% formic
608 acid, .01% ammonium hydroxide) to solvent B (70% isopropanol, 30% methanol, .02% formic
609 acid, .01% ammonium hydroxide) as previously described (*52*). Following chromatography, the
610 sample underwent electrospray ionization at 325°C with 5 L/min drying gas flow at 5500 V and
611 30 psig nebulizer pressure and ions were detected by time-of-flight in both positive and negative
612 modes (m/z range: 100 – 3000). Internal calibrants (922.009798 positive mode, 983.0325
613 negative mode) were infused continuously.

614 Lipids were identified using unique mass-retention time identifiers for masses exhibiting the
615 expected isotopic distributions as previously reported (*52*). Integrations of ion abundance were
616 determined using Agilent Profinder 8.0 and Qualitative Analysis 6.0.

617

618 **Growth curves**

619 Mtb strains were inoculated from frozen glycerol stocks and grown with appropriate selection
620 antibiotics in 7H9 medium until mid-log phase at 37°C.

621 For pre-depletion of iron internal stores, bacteria were washed in PBS or iron-chelated 7H9 and
622 diluted to an OD_{580nm} of 0.05 in iron-chelated 7H9. After 4-5 generations, bacteria were spun down
623 at 800rpm for 8 minutes to generate a single cell suspension. Bacteria were diluted to an OD_{580nm}
624 of 0.025 in the indicated media and added to flasks which were incubated standing at 37°C. For
625 serial passaging, when cultures in high iron media reached stationary phase, low iron cultures
626 were spun down at 800rpm for 8 minutes to generate a single cell suspension and bacteria were
627 diluted to an OD_{580nm} of 0.025 in both high/low iron media. OD measurements from cultures in

628 flasks were performed in a spectrophotometer. For growth curves in low iron media without
629 detergent, iron pre-depleted cultures were washed in PBS or detergent-free iron-chelated 7H9,
630 diluted to an OD_{580nm} of 0.05 and 100µL of bacteria were added to a 96-well plate in triplicates.
631 OD measurements from plates were performed in a plate reader. Cultures grown in 96-well plates
632 were resuspended prior to OD_{580nm} readings.

633 For CRISPRi strains, cultures were split into two flasks and 200ng/mL of ATc added to one of the
634 flasks 2-3 days prior to setting up the growth curve to pre-deplete the gene of interest. Fresh ATc
635 (200ng/mL) was again added to the media (+ATc conditions) before distributing bacteria into
636 96/384-well plates in triplicates.

637

638 **Reverse transcription quantitative polymerase chain reaction (RT qPCR)**

639 Primers and probes for RT qPCR are listed in table S4. Primers and probes were ordered from
640 TIB MOLBIO, LLC. cDNA was generated using MluV reverse transcriptase (New England Biolabs)
641 and approximately 500ng of total RNA. Parallel no-reverse transcriptase reactions were prepared
642 as a control for residual genomic DNA. qPCR was performed in the LightCycler® 480 System
643 (Roche). The housekeeping gene *sigA* (Rv2703) was used as an internal control. *sigA* probes
644 were labeled with 5' LC760/3' BBQ. Probes targeting genes of interest were all labeled with 5'
645 6FAM/3' BBQ or 3' BHQ.

646

647 **Minimal inhibitory concentrations (MIC) assays**

648 Mtb strains were inoculated from frozen glycerol stocks and grown with appropriate selection
649 antibiotics in 7H9 medium until mid-log phase at 37°C. Bacteria were diluted to an OD_{580nm} of 0.01
650 in 7H9 and 50µL of bacteria were added to a 384-well plate in triplicates per antibiotic
651 concentration, or to triplicate control wells without antibiotics. The HP D300e digital dispenser was
652 used to deliver antibiotics to plate wells. Bacteria were grown in standing cultures at 37°C and
653 OD_{580nm} was measured in a plate reader between days 10-21 following treatment (time point is
654 indicated in each figure legend). For MICs in low iron or detergent-free conditions, bacterial
655 cultures were first washed in PBS once or twice prior to dilution into the respective media of the
656 MIC assay. For CRISPRi strains, cultures were split into two flasks and 200ng/mL of ATc added
657 to one of the flasks 2-3 days prior to setting up the MIC assay to pre-deplete the gene of interest.

658 Fresh ATc (200ng/mL) was again added to the media of the assay (+ATc conditions) before
659 distributing bacteria into plates.

660

661 **Immunoprecipitation tandem mass spectrometry**

662 *Sample preparation*

663 Whole-cell lysates were collected from log-phase cultures grown in the shaking incubator,
664 incubated with 1% n-dodecyl -D-maltoside for 2h on a rotator at 4°C, followed by incubation with
665 anti-DYKDDDDK (FLAG) magnetic agarose (Pierce #A36797). Captured proteins were
666 dissociated from magnetic agarose by addition of 3x DYKDDDDK (3xFLAG) peptide (Pierce
667 #A36805), according to the manufacturer's instructions. Sodium Dodecyl Sulfate (SDS) was
668 added to the peptide eluate at a final concentration of 2% and samples were boiled at 95°C for
669 10 minutes. Boiled samples were transferred to protein lo-bind tubes. FLAG- (or 3xFLAG-) tagged
670 bait proteins were detected in eluates on an SDS-Polyacrylamide Gel Electrophoresis (PAGE) gel
671 prior to mass spectrometry.

672 23µg of proteins per sample were flash frozen on dry ice and subsequently dried using a Speed-
673 Vac. Next, 23µl of lysis buffer (5% SDS, 50mM TEAB) was added to initiate the S-Trap™ Micro
674 Spin digestion protocol (PROTIFI). The proteins underwent reduction by 4mM dithiothreitol (DTT)
675 and alkylation by 20mM iodoacetamide. Following an overnight digestion with trypsin at 37 °C,
676 peptides were eluted first by addition of 40µL of 50mM triethylammonium bicarbonate (TEAB) and
677 spun at 4000 rpm for 1 min. This was followed by a 1-minute spin with 40µL of 0.2% formic acid
678 (FA) and, lastly, 40µL of 50% acetonitrile (ACN). The three elution were then pooled together,
679 dried using a Speed-Vac, and reconstituted in 20µL of 0.1% FA in 5% ACN. After reconstitution,
680 the samples were centrifuged at 16,000 rpm for 16 min and an 18µL aliquot of the supernatant
681 was transferred to a non-binding HPLC vials.

682

683 *LC-MS/MS and data analysis workflows*

684 Data from the first experiment (pull-down of FecB-FLAG) was acquired on a TimsTOF Pro2
685 (Bruker) mass spectrometer, which was coupled to a nanoElute LC system from Bruker. 5µL of
686 peptides were loaded and separated on an in-house 75 µm I.D. fused silica analytical column
687 packed with 25-cm ReproSil-Pur C18-AQ (Dr. Maisch, GmbH, 120 Å, 3 µm) particles to a gravity-
688 pulled tip, using an aqueous mobile phase (A) of water and 0.1% FA and an organic mobile phase

689 (B) of ACN and 0.1% FA. A 30-minute gradient was employed for DDA-PASEF with a flow rate
690 set at 500 nL/min. The captive nano-electrospray voltage was maintained at 1600V, using one
691 column configuration (no trap). The DDA-PASEF method consists of 10 MS/MS PASEF scans per
692 topN acquisition cycle, with ramp and accumulation times of 100 ms, covering an m/z range from
693 100 to 1700 and an ion mobility range (1/K0) from 0.70 to 1.30 V s/cm^2. Collision energy settings
694 followed a linear function of ion mobility, ranging from 20 eV at 0.6 V s/cm^2 to 59 eV at 1.6 V
695 s/cm^2, using default parameters. Calibration of the instrument was performed using three ions
696 from the ESI-L Tuning Mix (Agilent) (m/z 622, 922, 1222).

697 The custom workflow 'LFQ-MBR' from FragPipe version 21.1 was used, including database
698 search with MSFragger (version 4.0), deep-learning prediction rescoring with MSBooster,
699 Percolator and ProteinProphet (Philosopher version 5.1.0) for PSM validation and protein
700 inference. The raw files from TimsTOF Pro2 were searched against the database
701 "Mycobacterium_tuberculosis_H37Rv_v4modified" appended with common contaminant
702 proteins. Decoy reversed sequences were appended to the search database. The default
703 MSFragger search parameters were used, except precursor and fragment mass tolerances were
704 set to 20 ppm; enzyme: trypsin (not cutting before P); peptide length 7-30. Variable modifications
705 were set to oxidation of Met and acetylation of protein N-t, and fixed modifications to
706 carbamidomethylation of Cys. MSBooster, Percolator and ProteinProphet default options were
707 used, and results were filtered by 1% FDR at protein level. The searched results were then
708 imported to Scaffold 5 Q+S (Proteome Software Inc., v5.3) for data visualization.

709 Data from the second experiment (pull-down of Rv3035-3xFLAG) was acquired using a
710 NanoAcquity UPLC (Waters Corporation, Milford, MA) coupled to an Orbitrap Fusion Lumos
711 Tribrid (Thermo Fisher Scientific, Waltham, MA) mass spectrometer. Peptides were trapped and
712 separated using an in-house packed precolumn packed with 2cm ReproSil-Pur C18-AQ (Dr.
713 Maisch, GmbH, 120 Å, 5 µm) particles plus and an in-house 75 µm I.D. fused silica analytical
714 column (as previously described) and the same solvent composition. 3.8µL sample was injected,
715 and the peptides were trapped at a flow rate of 4µL/min with 5% mobile phase B for 4 min, followed
716 by a gradient elution with 5-35% B at a flow rate of 300nL/min over 120 min (total run time 145
717 min). Mass spectra were acquired over m/z 375-1500 Da with a resolution of 120,000 (m/z 200).
718 Tandem mass spectra were acquired using data-dependent acquisition with an isolation width of
719 1.6 Da, HCD collision energy of 30%, resolution of 15,000 (m/z 200), maximum injection time of
720 50 ms, and an AGC target of 50,000.

721 Raw data files from the Orbitrap Fusion Lumos Tribrid were peak processed with Proteome
722 Discoverer (version 2.5, Thermo Scientific) followed by identification using Mascot Server (Matrix
723 Science, v2.6.2) against the same database used in the previous experiment. Search parameters
724 were as follows: tryptic digestion with up to 2 missed cleavages; peptide N-terminal acetylation,
725 methionine oxidation, and N-terminal glutamine to pyroglutamate conversion were specified as
726 variable modifications. Carbamidomethylation of cysteines was set as static modification.
727 Assignments were made using a 10-ppm mass tolerance for the precursor and 0.6 Da mass
728 tolerance for the fragment ions. All non-filtered search results were processed by Scaffold 5 Q+S
729 at 1.0% false-discovery rate (FDR) for peptides and 99% threshold for proteins (2 peptides
730 minimum).

731 For each experiment, Total Spectrum Count (TSC) was exported from Scaffold 5 Q+S into a
732 Microsoft Excel spreadsheet. Zeros were replaced with ones in WT control samples to allow fold-
733 change (FC) calculation of every protein detected in the samples containing the bait protein. For
734 normalization, we summed the TSC values for all proteins in each replicate, calculated the
735 average of the sum of the three replicates and divided the average by the sum value of each
736 replicate (this is the normalization factor). Then, we multiplied each protein TSC by the
737 normalization factor of that replicate sample, calculated the median, log2FC of tagged group over
738 WT control, and p-value by performing T-tests of the normalized values in each row. P-values
739 were transformed into -log10(p-value) for visualization of the data as a volcano plot.

740

741 **Co-essentiality analysis**

742 We performed co-essentiality analysis on CRISPR interference (CRISPRi) data (*13*), which
743 profiled Mtb fitness under 80 experimental conditions. These conditions span 9 antibiotics
744 (BDQ = bedaquiline; CLR = clarithromycin; EMB = ethambutol; INH = isoniazid;
745 LVX = levofloxacin; LZD = linezolid; RIF = rifampicin, STR = streptomycin; VAN = vancomycin),
746 each tested under 9 screening conditions defined by a combination of pre-depletion time (1, 5, or
747 10 days of CRISPRi induction before drug exposure) and drug concentration ("Low," "Medium,"
748 or "High" partially inhibitory doses). We used only the $\log_2$ fold change (LFC) values from negative
749 selection screens, which report the fitness effects of gene knockdown.

750 Each gene was thus represented by an 80-dimensional LFC vector capturing its essentiality
751 profile across the drug/time/concentration matrix. To account for covariance across screens—
752 such as batch effects—we computed an 80×80 empirical covariance matrix (Σ) from the LFC

753 data. We then applied generalized least squares (GLS), following a previously reported approach
754 (*53*) to compute pairwise co-essentiality relationships among 3,979 genes. This yielded a 3,979
755 × 3,979 matrix of GLS coefficients and corresponding p-values.

756 We corrected for multiple hypothesis testing using the Benjamini–Hochberg procedure
757 (fdrcorrection in the Python statsmodels package). Gene pairs with a false discovery rate (FDR)-
758 adjusted p-value < 0.001 were considered significantly co-essential, resulting in approximately
759 16,000 high-confidence gene pairs.

760

761 **Design of expression constructs for *M. thermoresistibile* (Mth) Rv3035**

762 Initial attempts to express Mtb Rv3035 in *E. coli* using N- or C-terminal 6xHis-tag (His) constructs
763 with full-length and various N-terminal truncations failed to produce soluble Rv3035. To improve
764 solubility, we turned to a thermostable homolog of Rv3035, Mth Rv3035, Accession no.
765 WP_040546537, and constructed two *E. coli* codon-optimized constructs cloned into pET28a with
766 a TEV-cleavable N-terminal His-tag (GenScript, Piscataway, NJ). The Mth Rv3035 construct that
767 encodes for the mature form of Rv3035 without its predicted signal peptide (SignalP 6.0 (*14*)),
768 starting at residue Gly2 (fig. S4B), produced soluble Rv3035 only when expressed in *E. coli*
769 T7SHuffle cells (New England Biolabs, Ipswich, MA). Notably, T7SHuffle cells promote disulfide
770 bond formation (*54*), and Rv3035 is predicted to harbor two disulfide bonds.

771

772 **Generation of FecB mutants for *in vitro* studies**

773 A pET28a FecB construct encoding Mtb FecB (without the signal peptide, mature FecB starting
774 at residue 39) with a thrombin-cleavable N-terminal 6xHis-tag (*7*) was used as the template for *in*
775 *vitro* site-directed mutagenesis using Pfu Ultra Fusion HS DNA polymerase (Agilent) with the
776 primers listed in table S5 and then confirmed by DNA sequencing (GeneWiz from Azenta Life
777 Sciences). The FecB construct encoding no His-tag was generated using the pET28a FecB
778 plasmid and excising the encoded *fecB* gene with *Nde*I and *BamH*I and ligating it into a pET22b
779 vector.

780

781 **Expression and purification of Mth Rv3035 and the Mth Rv3035-Mtb FecB complex**

782 Mth Rv3035-His was expressed in *E. coli* T7SHuffle cells in Terrific Broth (TB) media containing
783 0.4% glycerol and 50µg/mL kanamycin (Kan). To express the Mth Rv3035-Mtb FecB complex,
784 which we refer to as the FecB-Rv3035 complex throughout the manuscript, both pET28a Mth
785 Rv3035-His and pET22b Mtb FecB plasmids were co-transformed into T7SHuffle cells with
786 selection on LB + 50µg /mL Kan and 100µg/mL ampicillin (Amp) agar plates. A fresh transformant
787 was used to inoculate TB containing 0.4% glycerol, 50µg/mL Kan and 100µg/mL Amp. Cells were
788 grown at 37°C to an OD_{600nm} of ~ 0.6, before protein expression was induced by the addition of
789 0.5mM isopropyl β-D-1-thiogalactopyranoside (IPTG). The cells grown overnight at 20°C and
790 harvested by centrifugation.

791 Both Mth Rv3035-His and the FecB-Rv3035-His complex were purified using the same protocol.
792 Cell pellets were resuspended in 10x vol(mL)/w(g)of cells in Buffer A (150mM NaCl, 50mM Tris,
793 pH 7.8) with 0.25mM phenylmethylsulfonyl fluoride (PMSF) with stirring at 4°C for 30 minutes.
794 Cells were lysed by sonication and cell debris was pelleted by centrifugation at 14,000rpm for 1h
795 at 4°C. The cell lysate was passed through a 1µm syringe filter to remove insoluble debris and
796 applied to a His-trap column (Cytiva, Marlborough, MA) pre-equilibrated with Buffer A using an
797 AKTA Start FPLC instrument (Cytiva, Marlborough, MA). Following a 10x column volume (CV)
798 wash step with Buffer A, a gradient of Buffer A from 0 to 500mM imidazole over 20 CVs elute His-
799 tagged proteins. Fractions with containing Mth Rv3035-His or the FecB-Rv3035-His complex
800 were concentrated using an Amicon concentrator (MilliporeSigma, 30kDa cut-off) with buffer
801 exchange into Buffer A.

802

803 **Expression and purification of Mtb FecB and mutants**

804 Purification of WT FecB and FecB mutant proteins were carried out in a similar manner as
805 previously described (*7*). FecB WT or mutants were expressed in BL21-(DE3) cells and cells were
806 grown in TB + 0.4% glycerol + 50µg/mL Kan at 37°C to an OD_{600nm} of ~0.6, before protein
807 expression was induced with IPTG (0.5mM). Cell growth was continued overnight for 20h at 20°C,
808 before cells were harvested by centrifugation. Cell pellets were resuspended in 10x vol(mL)/w(g)
809 Buffer B (350 mM NaCl, 50 mM Tris, pH 7.8, 10% glycerol) with 0.25mM PMSF with stirring at
810 4°C for 30 minutes. Cells were lysed by sonication and cell debris was pelleted by centrifugation
811 at 14,000rpm for 1h at 4°C. The cell lysate was filtered and applied to a Ni-NTA resin pre-
812 equilibrated with Buffer B using gravity flow. The column was washed with Buffer B and eluted
813 with a stepwise elution gradient of imidazole going up to 600mM imidazole in Buffer B. Fractions

814 found to contain FecB by SDS-PAGE analysis (expected MW ~37 kDa) were pooled and dialyzed
815 against Buffer B overnight at 4°C.

816

817 **Removal of N-terminal His-tag from Rv3035-His and FecB-His**

818 For cleavage of His-tags from Rv3035-His and from the FecB-Rv3035-His complex, TEV was
819 added to approximately 30-100mg of protein at a final concentration ~0.1mg/ml TEV and
820 incubated overnight at 4°C. The cleavage reaction was passed over a Ni-NTA column pre-
821 equilibrated with Buffer A + 10mM imidazole and chased with Buffer A + 10mM imidazole. Flow-
822 through fractions containing Rv3035 or FecB-Rv3035 complex were concentrated and buffer
823 exchanged into Buffer A.

824 For the isolation of tag-free WT FecB, which was used for some ITC experiments, a similar
825 procedure was used but with thrombin at ~30U thrombin:1mg FecB-His. The cleavage reaction
826 was passed over a Ni-NTA column pre-equilibrated with Buffer B + 10mM imidazole and chased
827 with Buffer B + 10mM imidazole. Flow-through fractions containing WT FecB were concentrated
828 and buffer exchanged into Buffer B.

829

830 **Isothermal titration calorimetry (ITC) experiments**

831 ITC experiments were carried out using a Malvern MicroCal PEAQ-ITC instrument (Malvern,
832 United Kingdom). Prior to the experiments, proteins were dialyzed into Buffer B and the same
833 dialysis buffer was used for protein dilutions. 19-point titrations were carried out using 200μM Mth
834 R3035 in the syringe and 20μM FecB in the cell, whereas 13-point titrations were carried out using
835 300μM Rv3035 and 30μM FecB-His mutant protein, or 200μM Rv3035-His and 20μM FecB-His.
836 Notably, the His-tag on FecB did not appreciably change the affinity of FecB for Rv3035. Curve
837 fitting was carried out using the Malvern instrument analysis software.

838

839 **Structure determination of Mth Rv3035 and the FecB-Rv3035 complex**

840 Initial screening of Mth Rv3035 (15mg/mL) and FecB-Rv3035 complex (38mg/mL) were carried
841 out in 96-well trays using a Mosquito liquid handler (SPT Labtech, Cambridge, MA) and
842 commercially available crystallization screens by the hanging drop vapor diffusion method.

843

844 *Mth Rv3035 alone*

845 Diffraction-quality Mth Rv3035 crystals were grown with a crystallization reservoir of 0.1M sodium
846 chloride; 0.1M HEPES, pH 7.5; 1.6M ammonium sulfate with Rv3035 at 15 mg/mL and a reservoir
847 to protein ratio of 1:1 at room temperature. The crystals were cryocooled in mother liquor
848 supplemented with 25% glycerol. Data was collected at SSRL 12-2 at the wavelength 1 Å. Data
849 was processed in xds (*55*) to a resolution of 1.9 Å (table S1). A model of Mth Rv3035 was
850 generated on the AlphaFold server (*26*) and was used for molecular replacement (MR) in phaser
851 (*56*) in phenix. The MR solution placed two subunits in the asymmetric unit (ASU) and was
852 improved by autobuild in phenix (*57*), and refined in phenix.refine(*58*). Following autobuild, the N-
853 terminal residues 10-37 were built *de novo* in coot (*59*). The N-terminal 9 residues of Rv3035
854 could not be modeled for both subunits, and for subunit B, the last C-terminal residue also could
855 not be modeled due to unresolved electron density. The model was further refined in phenix.refine
856 and coot to a final R_{work}/R_{free} of 16.1 / 20.25 (table S1).

857

858 *FecB-Rv3035 complex*

859 Diffraction-quality crystals of the FecB-Rv3035 complex were obtained with a crystallization
860 reservoir of 3M sodium chloride; 0.1M Bis-Tris, pH 7.0 with a reservoir to protein complex ratio of
861 1: 1. To further improve diffraction quality of the FecB-Rv3035 complex, an additive screen was
862 performed (Hampton Research, Aliso Viejo, CA), with the final conditions used being a
863 crystallization reservoir of 3M sodium chloride; 0.1M Bis-Tris, pH 7.0; 3% trehalose, with the
864 Rv3035-FecB complex at 38mg/ml and a reservoir to protein ratio of 1:1. Crystals were
865 cryoprotected in reservoir solution with 25% glycerol and flash frozen with liquid nitrogen. Data
866 was collected at SSRL 12-2 at the wavelength 1 Å.

867 Data was processed in XDS (*55*) to a resolution of 3.3 Å (table S1). The phases were solved by
868 MR in phaser (*56*) in phenix, placing a single subunit of the deposited FecB structure (PDB ID
869 7UQ0,(*7*)) in the ASU in complex with a single subunit of the Mth Rv3035 structure solved above.
870 The MR solution was improved in autobuild and refined as described above in phenix.refine (*58*)
871 and coot (*59*) to a final R_{work}/R_{free} of 25.2/26.3 (table S1).

872

873 **Knockout construction**

874 Δ*rv3035* and Δ*fecB*Δ*rv3035* mutants were generated using a suicide plasmid approach as
875 previously described (*60*) with a few modifications. Constructs containing 500bp fragments
876 corresponding to regions upstream and downstream of *rv3035* were ordered from GenScript and
877 cloned into a temperature-sensitive deletion vector pDE43-XSTS to flank the zeocin resistance
878 cassette and generate pKO-XSTS-Zeo-*rv3035* via Gateway Cloning. Mtb WT and Δ*fecB* were
879 transformed with both the pKO-XSTS-Zeo-*rv3035* and a *rv3035* complementation plasmid
880 (pGMCS-T02-P*hsp60*-SD1-*rv3035*_A-HA) to generate a merodiploid strain since initial attempts
881 of generating the knockout with pKO-XSTS-Zeo-*rv3035* alone had failed. Transformants were
882 plated on Middlebrook 7H10 agar (BD #262710) containing 0.5% glycerol, 10% OADC (BD
883 #212351) and 25µg/mL Zeo (for WT) or 50µg/mL Hyg and 25µg/mL Zeo (for Δ*fecB*) and incubated
884 at 37°C until colonies were approx. 1mm in diameter. Colonies were tested for reporter gene XylE
885 activity directly on plates by addition of a drop of catechol solution (1g in 20mL water). After 30
886 minutes, candidate colonies that turned yellow were selected and grown in regular 7H9 with
887 appropriate antibiotics until they reached an OD_{580nm} of 1-1.5. Candidates were then grown on
888 7H10 agar with 10% sucrose at 37°C until colonies were approx. 1mm in diameter. Colonies were
889 test for reporter gene activity as above, but this time white colonies (that had successfully lost the
890 suicide plasmid) were selected. Genomic DNA (gDNA) was extracted from a few mutant
891 candidates and allelic exchange was confirmed by PCR using primers listed in table S6. To obtain
892 the final knockout mutants, we replaced the *rv3035* complementation plasmid integrated into attL5
893 with an empty plasmid containing an apramycin resistance cassette (pGMCA-OXOX).
894 Transformants were plated on 7H10 containing Zeo (or Zeo and Hyg) and 60µg/mL apramycin.
895 Δ*rv3035* and Δ*fecB*Δ*rv3035* mutants took about 6-8 weeks to form visible colonies. Candidate
896 mutants were selected and tested for streptomycin sensitivity in liquid culture as an indication that
897 the copy of *rv3035* (carrying streptomycin resistance) was successfully replaced in attL5. Finally,
898 gDNA was extracted for whole genome sequencing to confirm deletion of *rv3035* and insertion of
899 zeocin and apramycin cassettes.

900

901 **Cell envelope permeability assays**

902 BODIPY Fluorescent (FL) vancomycin (Invitrogen #V34850) uptake was performed as previously
903 reported (*5*) with a few modifications. Briefly, mid-log phase Mtb cultures were washed once and
904 adjusted to an OD_{580nm} of 2 in PBS and incubated with 2µg/mL of BODIPY FL vancomycin. 350µL
905 sample aliquots were taken at the 30 minutes incubation time point, washed twice in PBS 0.05%
906 Tween80, and resuspended in 350µL PBS. Negative control samples were treated the same way

907 but did not receive BODIPY FL vancomycin. 100µL of each sample was distributed in triplicate
908 wells in a black-sided 96-well plate. Fluorescence was measured (excitation wavelength of 485nm
909 and emission wavelength of 538nm) and normalized to the OD_{580nm} of the final suspension to
910 account for cell loss during washing steps.

911 For the calcein-AM (Invitrogen #C3099) uptake assay, mid-log phase cultures were adjusted to
912 an OD_{580nm} of 0.8 in regular 7H9 and 100µL aliquots were added to the wells of a black-sided 96-
913 well plate in triplicates. 100µL of calcein-AM (1µg/mL in 7H9 0.4% glucose) was added to the
914 wells resulting in a final concentration of 0.5µg/mL calcein-AM. Fluorescence was measured
915 (excitation wavelength of 495nm and emission wavelength of 520nm) at 2 minutes intervals over
916 a course of 60 minutes. Fluorescence was normalized to OD_{580nm} measured at 60 minutes.

917

918 **Spot assay**

919 Mig-log phase Mtb cultures were adjusted to an OD_{580nm} of 0.3 and 10-fold serial dilutions in PBS
920 0.05% Tween80 were spotted on 7H10 agar with 5µL per spot. Plates were incubated at 37°C
921 and imaged after 2-3 weeks. To confirm colony morphology alteration and growth defect of Δ*fecB*,
922 Δ*rv3035* and Δ*fecB* Δ*rv3035* mutants, plates were incubated for 4-5 additional weeks, after which
923 the phenotypes were unchanged.

924

925 **DMN-Tre labeling and flow cytometry**

926 Mid-log phase Mtb cultures were adjusted to OD_{580nm} of 0.5 in regular 7H9. For CRISPRi strains,
927 cultures were split into two flasks and 200ng/mL of ATc was added to one of the flasks 2-3 days
928 prior to labeling with DMN-Tre to pre-deplete the gene of interest. DMN-Tre probe (*31*) was added
929 to 500µL of culture at a final concentration of 100µM. Samples were incubated at 37°C overnight
930 for approximately 20h. On the next day, cultures were spun down at 10,000rpm for 3 minutes,
931 and the supernatant containing DMN-Tre was discarded. Samples were fixed with 4% PFA
932 (Biolegend #420801) for 4h at room temperature. After two washes in PBS 0.05% Tween80,
933 bacteria were resuspended in PBS. Data collection was performed on a FACSymphony A5 Cell
934 Analyzer (BD Biosciences) at the Weill Cornell Medicine Flow Cytometry Core Facility using the
935 405nm violet laser and the 405 [425/50] detector. Fluorescence data were obtained for 200,000
936 events per sample and analyzed in FlowJo software (BD) by first gating on the bacterial population

937 in the side scatter versus forward scatter plot followed by calculation of the mean fluorescence
938 intensity.

939

940 **Preparation and analysis of lipoglycans and arabinogalactan**

941 Lipoglycan and mycolyl-arabinogalactan-peptidoglycan (mAGP) complex extraction from
942 delipidated cells followed earlier procedures (*61*, *62*). Determination of the glycosyl linkage
943 patterns of lipoglycans and mAGP followed earlier procedures (*61*). Per-*O*-methylated alditol
944 acetates were analyzed by GC/MS on a Thermo Scientific TRACE 1310 Gas Chromatograph
945 paired with a Thermo Scientific TSQ 8000 Evo Triple Quadrupole GC-MS/MS. Samples were run
946 on a Zebron ZB-5HT Inferno 30 m x 0.25 mm x 0.25 µm capillary column (Phenomenex) at an
947 initial temperature of 100°C. The temperature was increased to 150°C at a ramp rate of 20°C min^{-}
948 ^{1}, then to 240°C at a ramp rate of 5°C min^{-1} and was held at this temperature for 3 min to be finally
949 increased to 300°C at a rate of 30°C min^{-1} and held at the final temperature for 5 min. Data
950 handling was carried out using the Thermo Scientific Chromeleon Chromatography Data System
951 software.

952

953 **Mouse infection**

954 Sixty-four female, eight-week-old *Mus musculus* C57BL/6 (Jackson Laboratories) were infected
955 with ~100 colony forming units (CFU)/mouse using an Inhalation Exposure System (Glas-Col).
956 Mice in the doxycycline group started to receive doxycycline chow 2 days before aerosol infection.
957 The FecB-TetON strain was grown to mid-log phase in the presence of 1µg/mL ATc, a single cell
958 suspension was prepared in PBS 0.05% Tween80 and then resuspended in PBS for a final
959 OD_{580nm} of 0.2. Lungs and spleen were homogenized in PBS and plated on 7H10 agar containing
960 1µg/mL ATc to determine CFU/organ at the indicated time points. This experiment was performed
961 in accordance with the Guide for the Care and Use of Laboratory Animals of the National Institutes
962 of Health, with approval from the Institutional Animal Care and Use Committee of Weill Cornell
963 Medicine.

964

965 **Quantification and statistical analysis**

966 Data analysis and generation of graphs were performed in Prism version 10.5 (GraphPad).

967

968 **References**

969 1. Geneva: World Health Organization, Global Tuberculosis Report 2024. License: CC BY-
970 NC-SA 3.0 IGO. (2024).

971 2. N. C. Poulton, J. M. Rock, Unraveling the mechanisms of intrinsic drug resistance in
972 Mycobacterium tuberculosis. Front Cell Infect Microbiol 12, 997283 (2022).

973 3. C. L. Dulberger, E. J. Rubin, C. C. Boutte, The mycobacterial cell envelope - a moving
974 target. Nat Rev Microbiol 18, 47–59 (2020).

975 4. M. Jackson, C. M. Stevens, L. Zhang, H. I. Zgurskaya, M. Niederweis, Transporters
976 Involved in the Biogenesis and Functionalization of the Mycobacterial Cell Envelope. Chem
977 Rev 121, 5124–5157 (2020).

978 5. W. Xu, M. A. Dejesus, N. Rücker, C. A. Engelhart, M. G. Wright, C. Healy, K. Lin, R. Wang,
979 S. W. Park, T. R. Ioerger, D. Schnappinger, S. Ehrt, Chemical Genetic Interaction Profiling
980 Reveals Determinants of Intrinsic Antibiotic Resistance in Mycobacterium tuberculosis. doi:
981 10.1128/AAC.01334-17 (2017).

982 6. H. Staudenmaier, B. Van Hove, Z. Yaraghi, V. Braun, Nucleotide sequences of the
983 fecBCDE genes and locations of the proteins suggest a periplasmic-binding-protein-
984 dependent transport mechanism for iron(III) dicitrate in Escherichia coli. J Bacteriol 171,
985 2626–2633 (1989).

986 7. R. de Miranda, B. J. Cuthbert, T. Klevorn, A. Chao, J. Mendoza, M. Arbing, P. J. Sieminski,
987 K. Papavinasasundaram, S. Abdul-Hafiz, S. Chan, C. M. Sassetti, S. Ehrt, C. W. Goulding,
988 Differentiating the roles of Mycobacterium tuberculosis substrate binding proteins, FecB
989 and FecB2, in iron uptake. PLoS Pathog 19 (2023).

990 8. L. Wang, E. Asare, A. C. Shetty, F. Sanchez-Tumbaco, M. R. Edwards, R. Saranathan, B.
991 Weinrick, J. Xu, B. Chen, A. Bénard, G. Dougan, D. W. Leung, G. K. Amarasinghe, J. Chan,
992 C. F. Basler, W. R. Jacobs, J. A. M. Tufariello, Multiple genetic paths including massive
993 gene amplification allow Mycobacterium tuberculosis to overcome loss of ESX-3 secretion
994 system substrates. Proc Natl Acad Sci U S A 119, e2112608119 (2022).

995 9. G. Leisching, R. D. Pietersen, I. Wiid, B. Baker, Virulence, biochemistry, morphology and
996 host-interacting properties of detergent-free cultured mycobacteria: An update.
997 Tuberculosis 100, 53–60 (2016).

998 10. D. Alland, A. J. Steyn, T. Weisbrod, K. Aldrich, W. R. Jacobs, Characterization of the
999 Mycobacterium tuberculosis iniBAC promoter, a promoter that responds to cell wall
1000 biosynthesis inhibition. J Bacteriol 182, 1802–1811 (2000).

1001 11. M. Schapira, M. Tyers, M. Torrent, C. H. Arrowsmith, WD40 repeat domain proteins: a novel
1002 target class? Nature Reviews Drug Discovery 2017 16:11 16, 773–786 (2017).

1003 12. A. Jinich, S. Z. Nazia, A. V. Tellez, A. M. Wu, R. Almada-Monter, C. M. Smith, K. Rhee,
1004 Genome-wide co-essentiality analysis in Mycobacterium tuberculosis reveals an itaconate
1005 defense enzyme module. bioRxiv, 2022.09.27.509804 (2022).

1006 13. S. Li, N. C. Poulton, J. S. Chang, Z. A. Azadian, M. A. DeJesus, N. Ruecker, M. D.
1007 Zimmerman, K. A. Eckartt, B. Bosch, C. A. Engelhart, D. F. Sullivan, M. Gengenbacher, V.
1008 A. Dartois, D. Schnappinger, J. M. Rock, CRISPRi chemical genetics and comparative
1009 genomics identify genes mediating drug potency in Mycobacterium tuberculosis. Nature
1010 Microbiology 2022 7:6 7, 766–779 (2022).

1011 14. F. Teufel, J. J. Almagro Armenteros, A. R. Johansen, M. H. Gíslason, S. I. Pihl, K. D.
1012 Tsirigos, O. Winther, S. Brunak, G. von Heijne, H. Nielsen, SignalP 6.0 predicts all five
1013 types of signal peptides using protein language models. Nature Biotechnology 2022 40:7
1014 40, 1023–1025 (2022).

1015 15. L. Smithers, S. Olatunji, M. Caffrey, Bacterial Lipoprotein Posttranslational Modifications.
1016 New Insights and Opportunities for Antibiotic and Vaccine Development. Front Microbiol 12,
1017 788445 (2021).

1018 16. M. G. Drage, H. C. Tsai, N. D. Pecora, T. Y. Cheng, A. R. Arida, S. Shukla, R. E. Rojas, C.
1019 Seshadri, D. B. Moody, W. H. Boom, J. C. Sacchettini, C. V. Harding, Mycobacterium
1020 tuberculosis lipoprotein LprG (Rv1411c) binds triacylated glycolipid agonists of Toll-like
1021 receptor 2. Nat Struct Mol Biol 17, 1088–1095 (2010).

1022 17. L. Holm, P. Rosenström, Dali server: conservation mapping in 3D. Nucleic Acids Res 38,
1023 W545–W549 (2010).

1024 18. M. A. Dejesus, E. R. Gerrick, W. Xu, S. W. Park, J. E. Long, C. C. Boutte, E. J. Rubin, D.
1025 Schnappinger, S. Ehrt, S. M. Fortune, C. M. Sassetti, T. R. Ioerger, Comprehensive
1026 essentiality analysis of the Mycobacterium tuberculosis genome via saturating transposon
1027 mutagenesis. mBio 8 (2017).

1028 19. B. Bosch, M. A. DeJesus, N. C. Poulton, W. Zhang, C. A. Engelhart, A. Zaveri, S. Lavalette,
1029 N. Ruecker, C. Trujillo, J. B. Wallach, S. Li, S. Ehrt, B. T. Chait, D. Schnappinger, J. M.
1030 Rock, Genome-wide gene expression tuning reveals diverse vulnerabilities of M.
1031 tuberculosis. Cell 184, 4579-4592.e24 (2021).

1032 20. E. Hesper Rego, R. E. Audette, E. J. Rubin, Deletion of a mycobacterial divisome factor
1033 collapses single-cell phenotypic heterogeneity. Nature 546, 153–157 (2017).

1034 21. M. Seidel, L. J. Alderwick, H. L. Birch, H. Sahm, L. Eggeling, G. S. Besra, Identification of a
1035 Novel Arabinofuranosyltransferase AftB Involved in a Terminal Step of Cell Wall Arabinan
1036 Biosynthesis in Corynebacterianeae, such as Corynebacterium glutamicum and
1037 Mycobacterium tuberculosis. Journal of Biological Chemistry 282, 14729–14740 (2007).

1038 22. Y. Liu, C. M. Brown, S. Erramilli, Y.-C. Su, S.-Y. Guu, P.-S. Tseng, Y.-J. Wang, N. H. Duong,
1039 P. Tokarz, B. Kloss, C.-R. Han, H.-Y. Chen, J. Rodrigues, K.-H. Khoo, M. Archer, A. A.
1040 Kossiakoff, T. L. Lowary, P. J. Stansfeld, R. Nygaard, F. Mancia, Structural insights into

terminal arabinosylation of mycobacterial cell wall arabinan. Nature Communications 2025 16:1 16, 1–16 (2025).

23. N. C. Poulton, J. M. Rock, Unraveling the mechanisms of intrinsic drug resistance in Mycobacterium tuberculosis. Front Cell Infect Microbiol 12, 997283 (2022).

24. K. R. Gupta, C. M. Gwin, K. C. Rahlwes, K. J. Biegas, C. Wang, J. H. Park, J. Liu, B. M. Swarts, Y. S. Morita, E. Hesper Rego, An essential periplasmic protein coordinates lipid trafficking and is required for asymmetric polar growth in mycobacteria. Elife 11 (2022).

25. M. Daffé, The mycobacterial antigens 85 complex – from structure to function and beyond. Trends Microbiol 8, 438–440 (2000).

26. J. Abramson, J. Adler, J. Dunger, R. Evans, T. Green, A. Pritzel, O. Ronneberger, L. Willmore, A. J. Ballard, J. Bambrick, S. W. Bodenstein, D. A. Evans, C. C. Hung, M. O'Neill, D. Reiman, K. Tunyasuvunakool, Z. Wu, A. Žemgulytė, E. Arvaniti, C. Beattie, O. Bertolli, A. Bridgland, A. Cherepanov, M. Congreve, A. I. Cowen-Rivers, A. Cowie, M. Figurnov, F. B. Fuchs, H. Gladman, R. Jain, Y. A. Khan, C. M. R. Low, K. Perlin, A. Potapenko, P. Savy, S. Singh, A. Stecula, A. Thillaisundaram, C. Tong, S. Yakneen, E. D. Zhong, M. Zielinski, A. Žídek, V. Bapst, P. Kohli, M. Jaderberg, D. Hassabis, J. M. Jumper, Accurate structure prediction of biomolecular interactions with AlphaFold 3. Nature 630, 493–500 (2024).

27. G. Degiacomi, A. Benjak, J. Madacki, F. Boldrin, R. Provvedi, G. Palù, J. Kordulakova, S. T. Cole, R. Manganelli, Essentiality of mmpL3 and impact of its silencing on Mycobacterium tuberculosis gene expression. Sci Rep 7, 1–8 (2017).

28. A. Fay, N. Czudnochowski, J. M. Rock, J. R. Johnson, N. J. Krogan, O. Rosenberg, M. S. Glickman, Two accessory proteins govern MmpL3 mycolic acid transport in mycobacteria. mBio 10 (2019).

29. C. Varela, D. Rittmann, A. Singh, K. Krumbach, K. Bhatt, L. Eggeling, G. S. Besra, A. Bhatt, MmpL Genes Are Associated with Mycolic Acid Metabolism in Mycobacteria and Corynebacteria. Chem Biol 19, 498–506 (2012).

30. R. Bansal-Mutalik, H. Nikaido, Quantitative lipid composition of cell envelopes of Corynebacterium glutamicum elucidated through reverse micelle extraction. Proc Natl Acad Sci U S A 108, 15360–15365 (2011).

31. M. Kamariza, P. Shieh, C. S. Ealand, J. S. Peters, B. Chu, F. P. Rodriguez-Rivera, M. R. Babu Sait, W. V. Treuren, N. Martinson, R. Kalscheuer, B. D. Kana, C. R. Bertozzi, Rapid detection of Mycobacterium tuberculosis in sputum with a solvatochromic trehalose probe. Sci Transl Med 10 (2018).

32. M. Jankute, L. J. Alderwick, S. Noack, N. Veerapen, J. Nigou, G. S. Besra, Disruption of mycobacterial aftB results in complete loss of terminal β(1 → 2) arabinofuranose residues of Lipoarabinomannan. ACS Chem Biol 12, 183–190 (2017).

1077 33. S. Gandotra, D. Schnappinger, M. Monteleone, W. Hillen, S. Ehrt, In vivo gene silencing
1078 identifies the Mycobacterium tuberculosis proteasome as essential for the bacteria to
1079 persist in mice. Nat Med 13, 1515–1520 (2007).

1080 34. K. A. Abrahams, G. S. Besra, Mycobacterial cell wall biosynthesis: a multifaceted antibiotic
1081 target. Parasitology 145, 116–133 (2018).

1082 35. R. Lissner, A. Franklin, S. T. Benedict, V. Charitou, A. Speer, J. Knol, C. Jimenez, P. J.
1083 Moynihan, S. Nejentsev, C. Kuijl, W. Bitter, A new role for lipoproteins LpqZ and FecB in
1084 orchestrating mycobacterial cell envelope biogenesis. bioRxiv, 2025.06.19.660376 (2025).

1085 36. Y. Liu, C. M. Brown, S. Erramilli, Y.-C. Su, S.-Y. Guu, P.-S. Tseng, Y.-J. Wang, N. H. Duong,
1086 P. Tokarz, B. Kloss, C.-R. Han, H.-Y. Chen, J. Rodrigues, K.-H. Khoo, M. Archer, A. A.
1087 Kossiakoff, T. L. Lowary, P. J. Stansfeld, R. Nygaard, F. Mancia, Structural insights into
1088 terminal arabinosylation of mycobacterial cell wall arabinan. Nature Communications 2025
1089 16:1 16, 1–16 (2025).

1090 37. O. Patel, R. Brammananth, W. Dai, S. Panjikar, R. L. Coppel, I. S. Lucet, P. K. Crellin,
1091 Crystal structure of the putative cell-wall lipoglycan biosynthesis protein LmcA from
1092 Mycobacterium smegmatis. Acta Crystallogr D Struct Biol 78, 494–508 (2022).

1093 38. M. Taschner, A. Mourão, M. Awasthi, J. Basquin, E. Lorentzen, Structural basis of outer
1094 dynein arm intraflagellar transport by the transport adaptor protein ODA16 and the
1095 intraflagellar transport protein IFT46. Journal of Biological Chemistry 292, 7462–7473
1096 (2017).

1097 39. T. Kanao, N. Hase, H. Nakayama, K. Yoshida, K. Nishiura, M. Kosaka, K. Kamimura, Y.
1098 Hirano, T. Tamada, Reaction mechanism of tetrathionate hydrolysis based on the crystal
1099 structure of tetrathionate hydrolase from Acidithiobacillus ferrooxidans. Protein Science 30,
1100 328–338 (2021).

1101 40. B. Jahn, A. Pol, H. Lumpe, T. R. M. Barends, A. Dietl, C. Hogendoorn, H. J. M. O. Den
1102 Camp, L. J. Daumann, Similar but Not the Same: First Kinetic and Structural Analyses of a
1103 Methanol Dehydrogenase Containing a Europium Ion in the Active Site. ChemBioChem 19,
1104 1147–1153 (2018).

1105 41. H. Yang, R. Yan, Y. Li, Z. Lu, X. Bie, H. Zhao, F. Lu, M. Chen, Structure-Function Analysis
1106 of a Quinone-Dependent Dehydrogenase Capable of Deoxynivalenol Detoxification. J Agric
1107 Food Chem 70, 6764–6774 (2022).

1108 42. M. Jackson, C. Raynaud, M. A. Lanéelle, C. Guilhot, C. Laurent-Winter, D. Ensergueix, B.
1109 Gicquel, M. Daffé, Inactivation of the antigen 85C gene profoundly affects the mycolate
1110 content and alters the permeability of the Mycobacterium tuberculosis cell envelope. Mol
1111 Microbiol 31, 1573–1587 (1999).

1112 43. J. O. Kilburn, K. Takayama, Effects of ethambutol on accumulation and secretion of
1113 trehalose mycolates and free mycolic acid in Mycobacterium smegmatis. Antimicrob Agents
1114 Chemother 20, 401–404 (1981).

1115 44. H. L. Birch, L. J. Alderwick, A. Bhatt, D. Rittmann, K. Krumbach, A. Singh, Y. Bai, T. L.
1116 Lowary, L. Eggeling, G. S. Besra, Biosynthesis of mycobacterial arabinogalactan:
1117 identification of a novel α(1→3) arabinofuranosyltransferase. Mol Microbiol 69, 1191 (2008).

1118 45. I. L. Sparks, T. Kado, M. Prithviraj, J. Nijjer, J. Yan, Y. S. Morita, Lipoarabinomannan
1119 mediates localized cell wall integrity during division in mycobacteria. Nature
1120 Communications 2024 15:1 15, 1–17 (2024).

1121 46. P. H. Culviner, C. K. Guegler, M. T. Laub, A simple, cost-effective, and robust method for
1122 rrna depletion in rna-sequencing studies. mBio 11 (2020).

1123 47. Y. Liao, G. K. Smyth, W. Shi, The R package Rsubread is easier, faster, cheaper and better
1124 for alignment and quantification of RNA sequencing reads. Nucleic Acids Res 47 (2019).

1125 48. S. Chen, Y. Zhou, Y. Chen, J. Gu, Fastp: An ultra-fast all-in-one FASTQ preprocessor.
1126 Bioinformatics 34, i884–i890 (2018).

1127 49. Y. Liao, G. K. Smyth, W. Shi, featureCounts: an efficient general purpose program for
1128 assigning sequence reads to genomic features. Bioinformatics 30, 923–930 (2014).

1129 50. M. I. Love, W. Huber, S. Anders, Moderated estimation of fold change and dispersion for
1130 RNA-seq data with DESeq2. Genome Biol 15, 1–21 (2014).

1131 51. M. Nandakumar, G. A. Prosser, L. P. S. De Carvalho, K. Rhee, Metabolomics of
1132 mycobacterium tuberculosis. Methods in Molecular Biology 1285, 105–115 (2015).

1133 52. E. Layre, L. Sweet, S. Hong, C. A. Madigan, D. Desjardins, D. C. Young, T. Y. Cheng, J. W.
1134 Annand, K. Kim, I. C. Shamputa, M. J. McConnell, C. A. Debono, S. M. Behar, A. J.
1135 Minnaard, M. Murray, C. E. Barry, I. Matsunaga, D. B. Moody, A Comparative Lipidomics
1136 Platform for Chemotaxonomic Analysis of Mycobacterium tuberculosis. Chem Biol 18,
1137 1537–1549 (2011).

1138 53. M. Wainberg, R. A. Kamber, A. Balsubramani, R. M. Meyers, N. Sinnott-Armstrong, D.
1139 Hornburg, L. Jiang, J. Chan, R. Jian, M. Gu, A. Shcherbina, M. M. Dubreuil, K. Spees, W.
1140 Meuleman, M. P. Snyder, M. C. Bassik, A. Kundaje, A genome-wide atlas of co-essential
1141 modules assigns function to uncharacterized genes. Nat Genet 53, 638–649 (2021).

1142 54. J. Lobstein, C. A. Emrich, C. Jeans, M. Faulkner, P. Riggs, M. Berkmen, SHuffle, a novel
1143 Escherichia coli protein expression strain capable of correctly folding disulfide bonded
1144 proteins in its cytoplasm. Microb Cell Fact 11, 1–16 (2012).

1145 55. W. Kabsch, XDS. Acta Crystallogr D Biol Crystallogr 66, 125–132 (2010).

1146 56. A. J. McCoy, R. W. Grosse-Kunstleve, P. D. Adams, M. D. Winn, L. C. Storoni, R. J. Read,
1147 Phaser crystallographic software. J Appl Crystallogr 40, 658–674 (2007).

1148 57. T. C. Terwilliger, R. W. Grosse-Kunstleve, P. V. Afonine, N. W. Moriarty, P. H. Zwart, L. W.
1149 Hung, R. J. Read, P. D. Adams, Iterative model building, structure refinement and density
1150 modification with the PHENIX AutoBuild wizard. Acta Crystallogr D Biol Crystallogr 64, 61–
1151 69 (2007).

58. P. V. Afonine, R. W. Grosse-Kunstleve, N. Echols, J. J. Headd, N. W. Moriarty, M. Mustyakimov, T. C. Terwilliger, A. Urzhumtsev, P. H. Zwart, P. D. Adams, Towards automated crystallographic structure refinement with phenix.refine. Acta Crystallogr D Biol Crystallogr 68, 352–367 (2012).

59. P. Emsley, K. Cowtan, Coot: Model-building tools for molecular graphics. Acta Crystallogr D Biol Crystallogr 60, 2126–2132 (2004).

60. U. Ganapathy, J. Marrero, S. Calhoun, H. Eoh, L. P. S. De Carvalho, K. Rhee, S. Ehrt, Two enzymes with redundant fructose bisphosphatase activity sustain gluconeogenesis and virulence in Mycobacterium tuberculosis. Nature Communications 2015 6:1 6, 1–12 (2015).

61. D. Kaur, M. R. McNeil, K. H. Khoo, D. Chatterjee, D. C. Crick, M. Jackson, P. J. Brennan, New Insights into the Biosynthesis of Mycobacterial Lipomannan Arising from Deletion of a Conserved Gene. Journal of Biological Chemistry 282, 27133–27140 (2007).

62. S. Bhamidi, M. S. Scherman, C. D. Rithner, J. E. Prenni, D. Chatterjee, K. H. Khoo, M. R. McNeil, The Identification and Location of Succinyl Residues and the Characterization of the Interior Arabinan Region Allow for a Model of the Complete Primary Structure of Mycobacterium tuberculosis Mycolyl Arabinogalactan. Journal of Biological Chemistry 283, 12992–13000 (2008).

63. A. Chao, C. W. Goulding, A Single Mutation in the Mycobacterium tuberculosis Heme-Degrading Protein, MhuD, Results in Different Products. Biochemistry 58, 489–492 (2019).

64. B. Thakuri, A. B. Graves, A. Chao, S. L. Johansen, C. W. Goulding, M. D. Liptak, The affinity of MhuD for heme is consistent with a heme degrading function in vivo. Metallomics 10, 1560–1563 (2018).

65. J. Schindelin, I. Arganda-Carreras, E. Frise, V. Kaynig, M. Longair, T. Pietzsch, S. Preibisch, C. Rueden, S. Saalfeld, B. Schmid, J. Y. Tinevez, D. J. White, V. Hartenstein, K. Eliceiri, P. Tomancak, A. Cardona, Fiji: An open-source platform for biological-image analysis. Nat Methods 9, 676–682 (2012).

66. S. Stael, L. P. Miller, Á. D. Fernández-Fernández, F. Van Breusegem, Detection of Damage-Activated Metacaspase Activity by Western Blot in Plants. Methods in Molecular Biology 2447, 127–137 (2022).

67. M. A. Conger, D. Pokhrel, M. D. Liptak, Tight binding of heme to Staphylococcus aureus IsdG and IsdI precludes design of a competitive inhibitor. Metallomics 9, 556–563 (2017).

68. L. Holm, P. Rosenström, Dali server: conservation mapping in 3D. Nucleic Acids Res 38, W545–W549 (2010).

69. J. Kim, H. Pham, Y. Baek, I. Jo, Y. H. Kim, N. C. Ha, Structure of the plant growth-promoting factor YxaL from the rhizobacterium Bacillus velezensis and its application to protein engineering. Acta Crystallogr D Struct Biol 78, 104–112 (2022).

70. M. Taschner, A. Mourão, M. Awasthi, J. Basquin, E. Lorentzen, Structural basis of outer dynein arm intraflagellar transport by the transport adaptor protein ODA16 and the intraflagellar transport protein IFT46. Journal of Biological Chemistry 292, 7462–7473 (2017).

71. T. Kanao, N. Hase, H. Nakayama, K. Yoshida, K. Nishiura, M. Kosaka, K. Kamimura, Y. Hirano, T. Tamada, Reaction mechanism of tetrathionate hydrolysis based on the crystal structure of tetrathionate hydrolase from Acidithiobacillus ferrooxidans. Protein Science 30, 328–338 (2021).

72. J. Baßler, H. Paternoga, I. Holdermann, M. Thoms, S. Granneman, C. Barrio-Garcia, A. Nyarko, G. Stier, S. A. Clark, D. Schraivogel, M. Kallas, R. Beckmann, D. Tollervey, E. Barbar, I. Sinning, E. Hurt, A network of assembly factors is involved in remodeling rRNA elements during preribosome maturation. Journal of Cell Biology 207, 481–498 (2014).

73. P. A. Lehner, M. Degen, R. P. Jakob, S. M. Modaresi, M. Callon, B. M. Burmann, T. Maier, S. Hiller, Architecture and conformational dynamics of the BAM-SurA holo insertase complex. Science Advances 11 (2025).

74. Z. Chen, L. H. Zhan, H. F. Hou, Z. Q. Gao, J. H. Xu, C. Dong, Y. H. Dong, Structural basis for the interaction of BamB with the POTRA3–4 domains of BamA. Acta Crystallographica Section D 72, 236–244 (2016).

75. B. Jahn, A. Pol, H. Lumpe, T. R. M. Barends, A. Dietl, C. Hogendoorn, H. J. M. O. Den Camp, L. J. Daumann, Similar but Not the Same: First Kinetic and Structural Analyses of a Methanol Dehydrogenase Containing a Europium Ion in the Active Site. ChemBioChem 19, 1147–1153 (2018).

76. P. Pausch, U. Singh, Y. L. Ahmed, B. Pillet, G. Murat, F. Altegoer, G. Stier, M. Thoms, E. Hurt, I. Sinning, G. Bange, D. Kressler, Co-translational capturing of nascent ribosomal proteins by their dedicated chaperones. Nature Communications 2015 6:1 6, 1–15 (2015).

77. C. Kuscu, M. Zaratiegui, H. S. Kim, D. A. Wah, R. A. Martienssen, T. Schalch, L. Joshua-Tor, CRL4-like Clr4 complex in Schizosaccharomyces pombe depends on an exposed surface of Dos1 for heterochromatin silencing. Proc Natl Acad Sci U S A 111, 1795–1800 (2014).

78. H. Yang, R. Yan, Y. Li, Z. Lu, X. Bie, H. Zhao, F. Lu, M. Chen, Structure-Function Analysis of a Quinone-Dependent Dehydrogenase Capable of Deoxynivalenol Detoxification. J Agric Food Chem 70, 6764–6774 (2022).

79. D. Schnappinger, K. M. O'Brien, S. Ehrt, Construction of conditional knockdown mutants in mycobacteria. Methods in Molecular Biology 1285, 151–175 (2015).

80. C. Ingram, M. Brawner, P. Youngman, J. Westpheling, xylE functions as an efficient reporter gene in Streptomyces spp.: Use for the study of galP1, a catabolite-controlled promoter. J Bacteriol 171, 6617–6624 (1989).

81. J.-M. Reyrat, V. Pelicic, B. Gicquel, R. Rappuoli, Counterselectable Markers: Untapped Tools for Bacterial Genetics and Pathogenesis. Infect Immun 66, 4011 (1998).

Acknowledgements

We thank Sae Woong Park (Weill Cornell Medicine) for sharing the Δ*mbtK* and Δ*mbtI* strains, Carolina Trujillo (Weill Cornell Medicine) for assistance with the animal experiment, and Allison Fay (Memorial Sloan Kettering Cancer Center) for her advice on the thin layer chromatography experiment. We thank the staff of the University of Massachusetts Chan Medical School Mass Spectrometry Facility and Kadamba Papavinasasundaram for their help with the immunoprecipitation tandem mass spectrometry experiments. We thank the Kamariza Lab at the University of California, Los Angeles for gifting an aliquot of the DMN-Tre probe. We thank the staff of the Weill Cornell Medicine Genomics Resources Core Facility and Flow Cytometry Core Facility for their contribution and advice on the RNA-seq and flow cytometry experiments, respectively. We thank the staff of the Advanced Light Source at Berkeley National Laboratories and the Stanford Synchrotron Radiation Lightsource for their invaluable help in data collection. We thank the Analytical Resources Core Facility at CSU (RRID: SCR_021758) for its help with GC/MS analyses.

Funding: This work was supported by the National Science Foundation Graduate Research Fellowship under grant No. 2139291 and a Potts Memorial Foundation Pre-Doctoral Fellowship (to T.K.). This work was also supported by the National Institute of Allergy and Infectious Diseases (NIAID)/ National Institutes of Health (NIH) grant AI155674 (to M.J.), grant K08AI148584 (to C.B.) and grant AI095208 (to C.W.G.). Additionally, this work was funded by the NIAID/NIH predoctoral training grant support AI141346 (to R.d.M. and J.M.). The content is solely the responsibility of the authors and does not necessarily represent the official views of the NIH.

Author contributions: Conceptualization: T.K., D.S. and S.E. Methodology: T.K., D.S. and S.E. Visualization: T.K. and S.E. Investigation: T.K., C.B., C.D.H., B.J.C., A.S., A.J., L.C., S.K.A., J.M., J.M., R.d.M. and H.K. Formal analysis: T.K. and S.E. Project administration: T.K. and S.E. Validation: T.K. Supervision: M.J., K.R., C.W.G. and S.E. Funding acquisition: T.K., M.J., C.B., C.W.G., R.d.M., J.M. and S.E. Writing—Original draft: T.K., C.D.H., B.J.C., M.J., C.W.G. and S.E. Writing—Review and editing: T.K., C.D.H., B.J.C., A.J., D.S., M.J., C.W.G. and S.E.

Competing interests: The authors declare that they have no competing interests.

Data and materials availability: All data needed to evaluate the conclusions in the paper are present in the paper and/or the Supplementary Materials. Bacterial strains generated in this paper will be provided upon request pending scientific review and a completed material transfer agreement. Requests should be directed to S.E. at sae2004@med.cornell.edu.

Figures

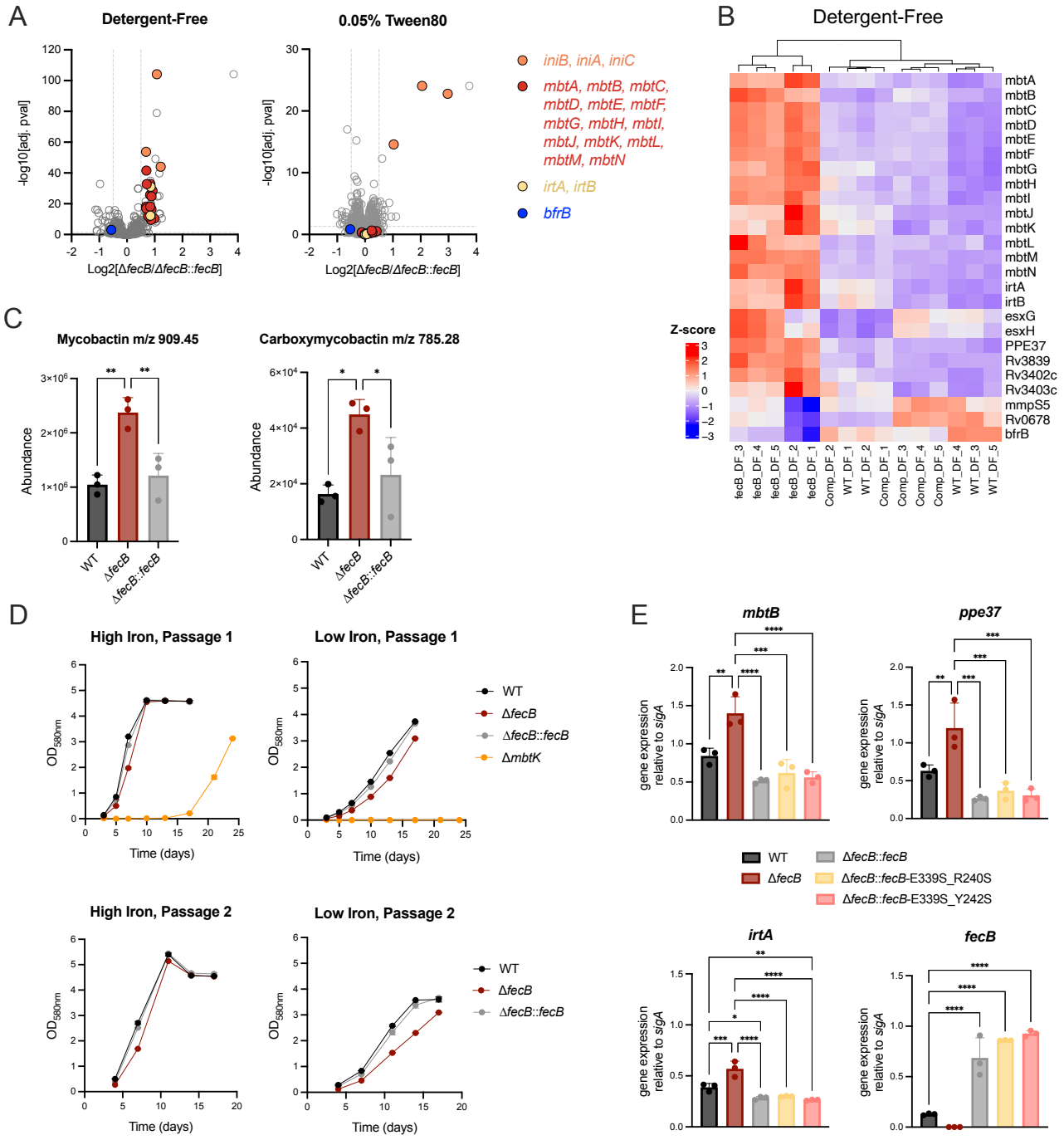

Figure 1. FecB plays a non-critical role in iron homeostasis in Mtb. (A) Volcano plots of transcriptome changes in Δ*fecB* compared to the complemented strain (Δ*fecB*::*fecB*) during log-phase growth in regular media without detergent or with 0.05% Tween80; highlighted genes are also differentially expressed in Δ*fecB* vs WT. (B) Heatmap of iron-related, differentially expressed genes (DEG) in strains grown in detergent-free media. DEGs were selected by padj ≤ 0.05 and |log2FC| ≥ 0.5; common hits in Δ*fecB* vs Δ*fecB*::*fecB* and Δ*fecB* vs WT are shown. (C) Relative

abundance of representative mycobactin and carboxymycobactin species detected as [M+Fe-2H]+ from lipid extracts analyzed by liquid chromatography-mass spectrometry (LC-MS). (D) Growth curves of iron pre-depleted strains in iron-chelated media with 160 µM (high iron) or 1 µM (low iron) ammonium ferric citrate (AFC). Cultures in low iron were grown until day 17 (Passage 1) and diluted to starting OD=0.025 in high/low iron media (Passage 2). Δ*mbtK* (mycobactin biosynthesis mutant) was used as a positive control that cannot grow in iron-limiting conditions. (E) Differential expression by reverse transcription quantitative PCR (RT qPCR) of representative iron-related genes (*mbtB*, *ppe37* and *irtA*) and *fecB* in strains grown in detergent-free media. Statistical significance in (C) and (E) was determined by one-way ANOVA and Tukey post-hoc test. Error bars: ±SD. **P* < 0.05; ***P* < 0.01; ****P* < 0.001; *****P* <0.0001. N independent experiments = 2 with a total of five replicate cultures (A-B), 2 (C), 5 (D) and 1 (E) each performed with triplicate cultures.

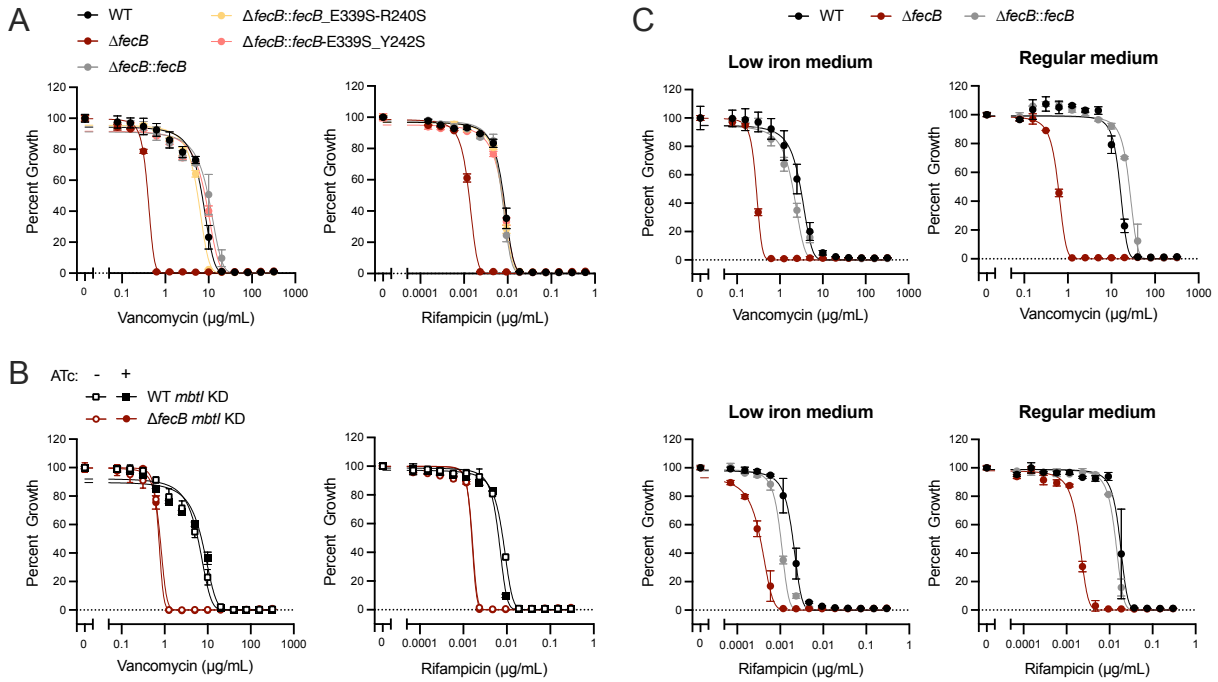

Figure 2. FecB's roles in iron homeostasis and multidrug resistance are not functionally related. MIC assays for vancomycin and rifampicin, percent growth calculated from no drug control wells. (A) Δ*fecB* complemented with FecB variants with lower binding affinity to ferric carboxymycobactin (Δ*fecB*::*fecB*-E339S_R240S and Δ*fecB*::*fecB*-E339S_Y242S) and control strains (day 14). (B) CRISPRi KD of *mbtI* in WT/Δ*fecB* in the absence or presence of ATc inducer (day 14). (C) WT, Δ*fecB* and Δ*fecB*::*fecB* strains in low iron (iron-chelated media with 1µM AFC) or regular media (day 21). Error bars: ±SD. N independent experiments = 2 (A, C), 1 (B), each performed with triplicate cultures.

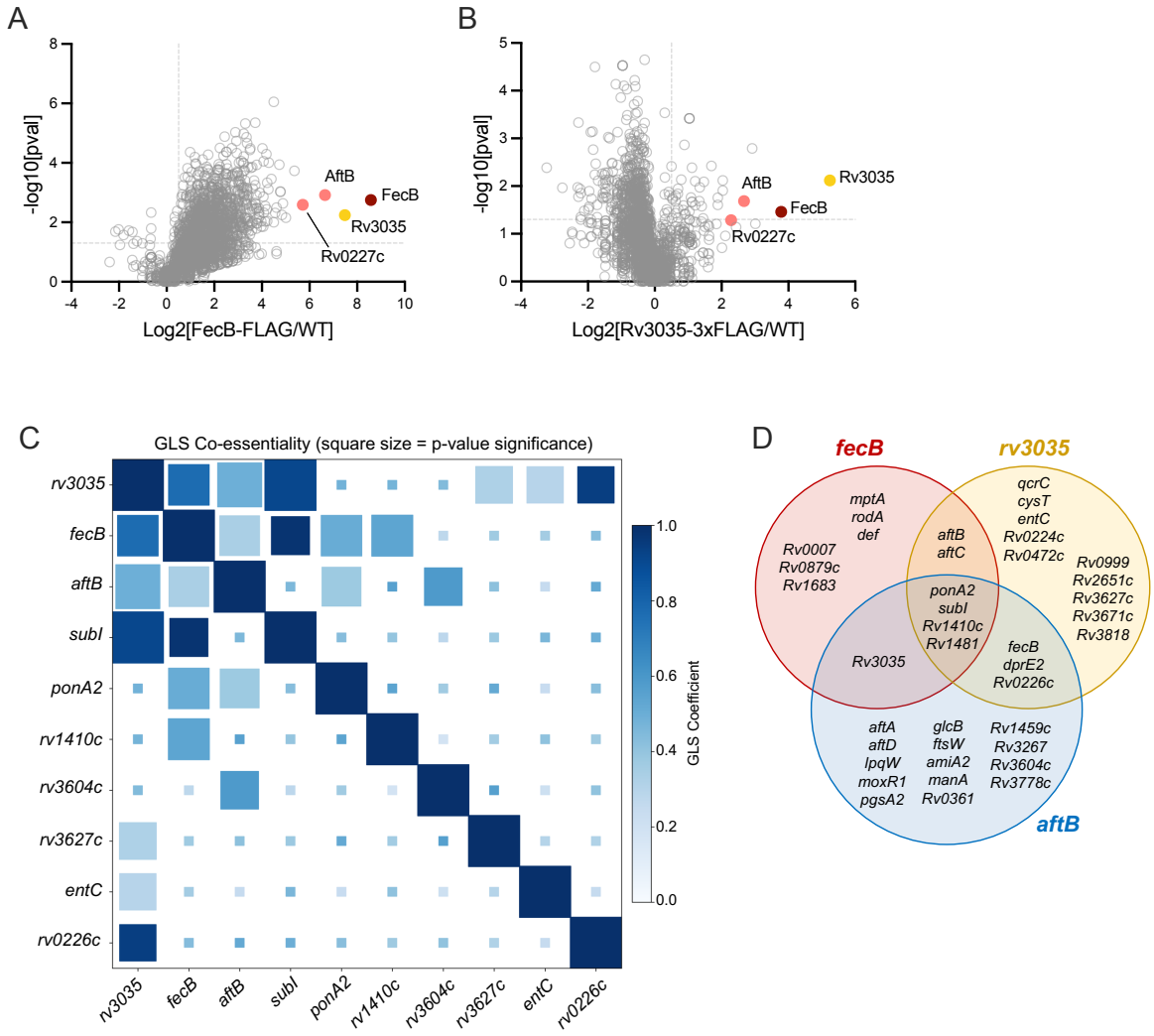

Figure 3. FecB and Rv3035 interact in Mtb and share essentiality profiles. Protein interaction profiling of (A) FecB and (B) Rv3035. FecB-FLAG and Rv3035-3xFLAG were immunoprecipitated from live Mtb and interacting proteins were identified by mass spectrometry. WT lysate was used a control for unspecific interactions. (C) Heatmap of co-essentiality Generalized Least Squares (GLS) coefficients for selected gene pairs. The genes shown were selected based on three "query genes": *fecB*, *rv3035*, and *aftB*. We included all gene pairs involving at least one of these queries that met a significance threshold of FDR-adjusted p-value < 0.001. Each square's color represents the GLS coefficient (i.e., the strength of co-essentiality), while size corresponds to statistical significance ($-\log_{10}$ of the FDR-adjusted p-value). Diagonal elements represent self-comparisons (each gene's $\log_2$ fold change profile against itself); while biologically uninformative, they are displayed at full size as a visual benchmark for perfect correlation. Some gene-gene combinations did not pass the significance threshold and are shown with smaller squares. (D) Venn diagram showing genes that are co-essential with *fecB* (red circle), *rv3035* (yellow circle) and *aftB* (blue circle), and their overlap. N independent experiments = 1 (A-B), each performed with triplicate cultures.

1333

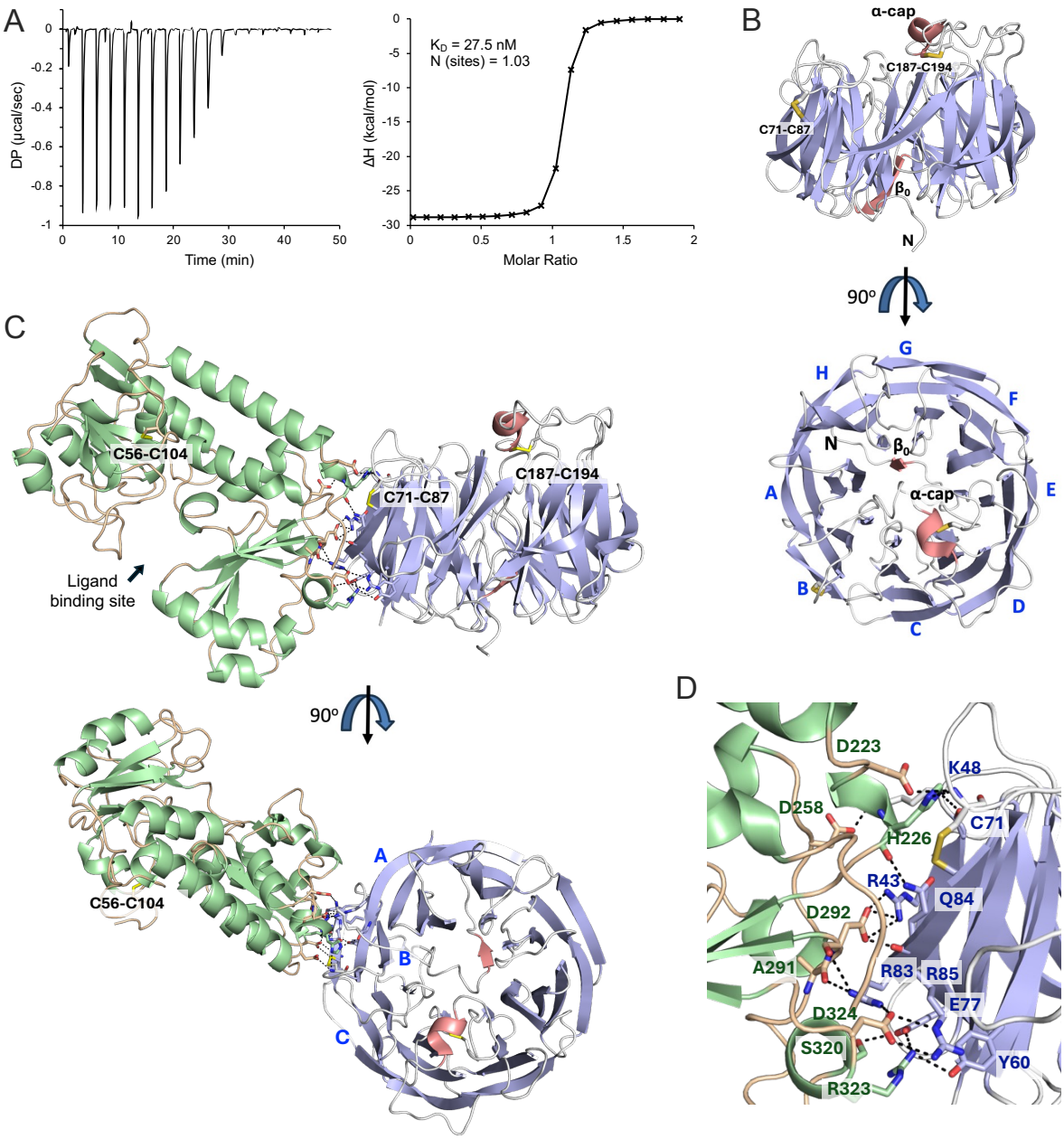

1334

1335 **Figure 4. Binding affinity of FecB and Rv3035 and X-ray crystal structures of Mth Rv3035**
1336 **and the FecB-Rv3035 complex.** (A) A 19-point ITC experiment was carried out by titrating 200µM
1337 Mth Rv3035 into 20µM Mtb FecB. The resulting thermogram is shown (left graph), resulting in the
1338 following calculated parameters: K_D = 27.5 ± 4.6 nM; N(sites) = 1.03 ± 0.004 (right graph). (B)
1339 Cartoon depiction of the structure of Mth Rv3035. The β-propeller fold is colored in light purple for
1340 β-strands and white for loops, each blade was assigned a letter, and the additional secondary
1341 structure elements are colored in pink. The disulfide bonds are shown in stick with yellow sulfur
1342 atoms. (C) Cartoon depiction of the structure of the FecB-Rv3035 complex. Rv3035 is colored as
1343 in (B). FecB secondary structure elements are colored in light green and loops in wheat. (D) A

zoom in of the interface of the FecB-Rv3035 complex with interacting residues shown in stick, and hydrogen bond and salt bridge interactions are represented in black dashed lines.

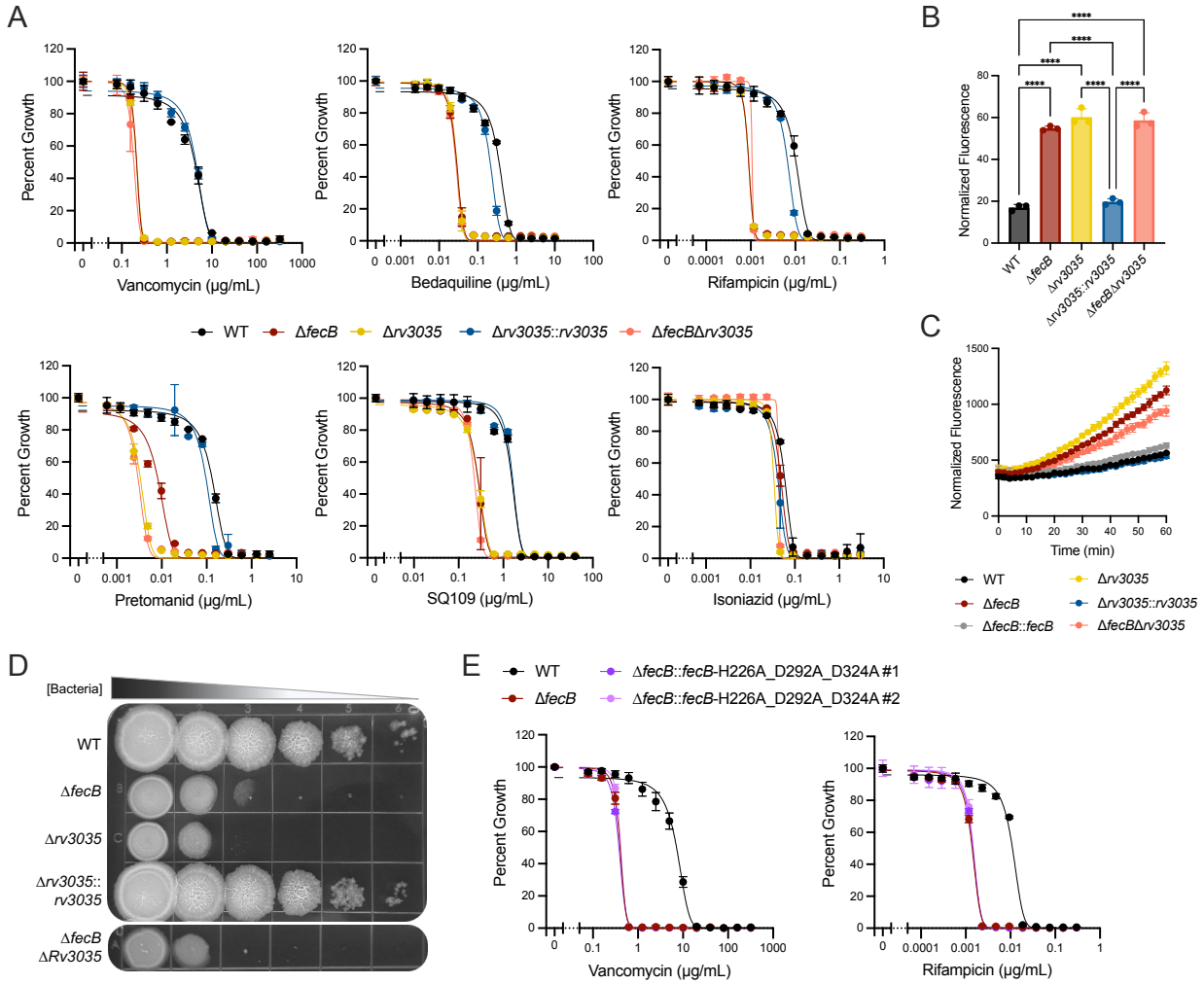

Figure 5. FecB and Rv3035 function in the same pathway that mediates cell envelope impermeability and antibiotic resistance in Mtb. (A) MIC assays for vancomycin, bedaquiline, rifampicin, pretomanid, SQ109 and isoniazid, percent growth calculated from no drug control wells (day 10). (B) BODIPY-vancomycin uptake after 30min of incubation, fluorescence intensity normalized by OD_{580nm}. Statistical significance was determined by one-way ANOVA and Tukey post-hoc test. (C) Calcein-AM uptake, fluorescence intensity normalized by OD_{580nm} at 60min. (D) Spot Assay. (E) MIC assay for vancomycin and rifampicin, percent growth calculated from no drug control wells. Δ*fecB* complemented with FecB triple mutant that does not bind Rv3035 (Δ*fecB*::*fecB*-H226A_D292A_D324A) and control strains (day 14), #1-2 indicate individual colonies (biological replicates). Error bars: ±SD. **P* < 0.05; ***P* < 0.01; ****P* < 0.001; *****P* <0.0001. N independent experiments = 2 (A-D), 1 (E), each performed with triplicate cultures.

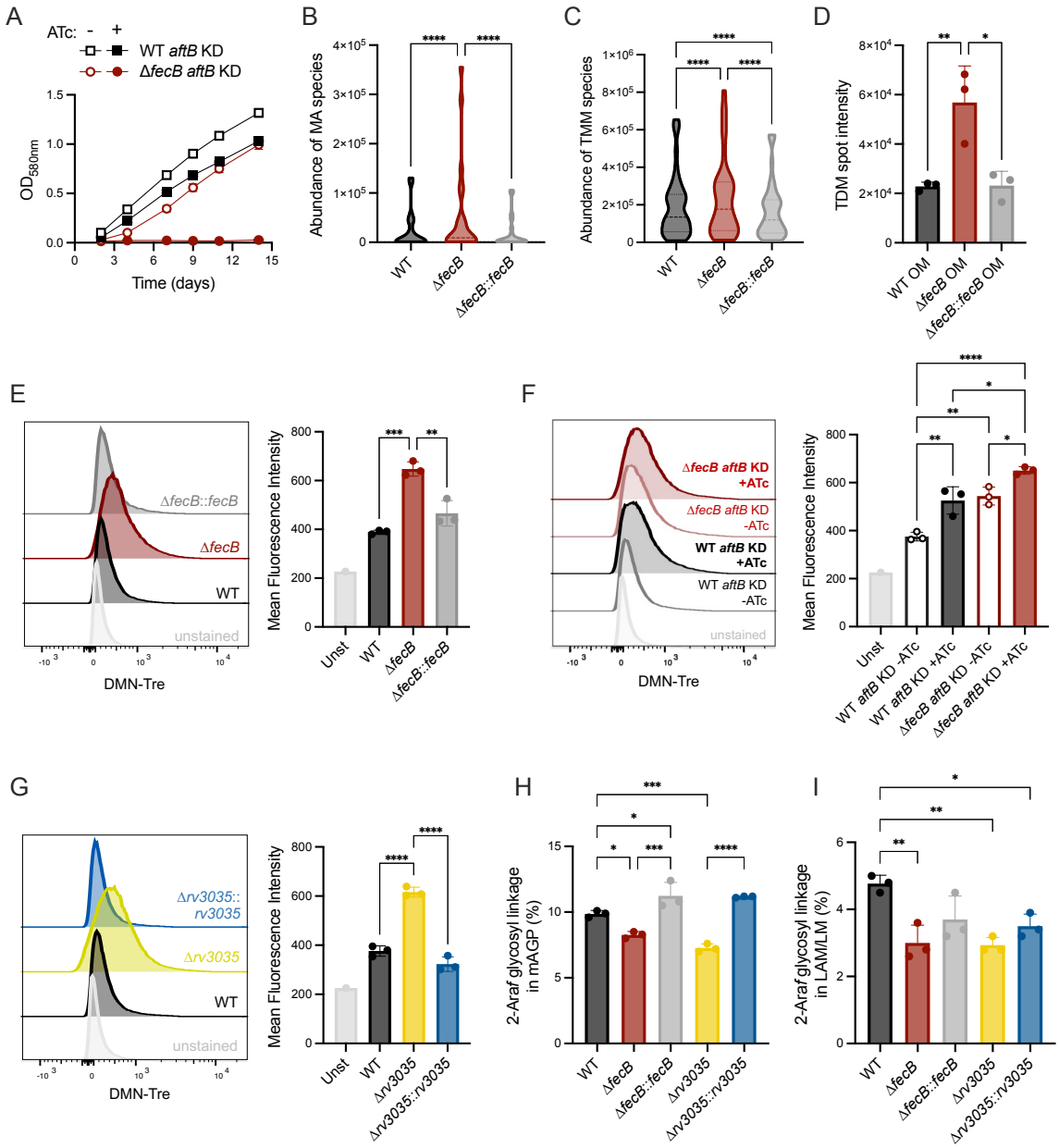

Figure 6. FecB and Rv3035 support AftB's function. (A) Growth curves of CRISPRi KD of *aftB* in WT/Δ*fecB* in the absence or presence of ATc inducer; strains were grown in 384-well plate in standing conditions. (B-C) Lipidomic analysis by LC-MS of total lipids identifying (B) free-mycolic acid (MA) species and (C) trehalose monomycolate (TMM) species. (D) Trehalose dimycolate (TDM) spot intensity quantified from fig. S13I by densitometry analysis using ImageJ software. OM refers to the outer leaflet of the outer membrane obtained after AOT treatment. (E-G) Flow cytometry analysis of DMN-Tre labelled cells using 405nm laser and 525/50 channel. Representative histograms (left) and quantification (right) of mean fluorescence intensity of DMN-Tre probe. Unstained (Unst) WT was used as a control for autofluorescence. (H-I) Relative percentage of 2-arabinofuranosyl (2-Ara*f*)-linked residues in (H) mAGP and (I) lipoglycans (LAM and LM mixture). See fig. S14 for full details of the glycosyl linkage analysis of mAGP and

LAM/LM. Statistical significance was determined by two-way (B-C) or one-way (D-I) ANOVA and Tukey post-hoc test. Error bars: ±SD. *P < 0.05; **P < 0.01; ***P < 0.001; ****P <0.0001. N independent experiments = 2 (A, E-G), 1 (B-D, H-I), each performed with triplicate cultures.

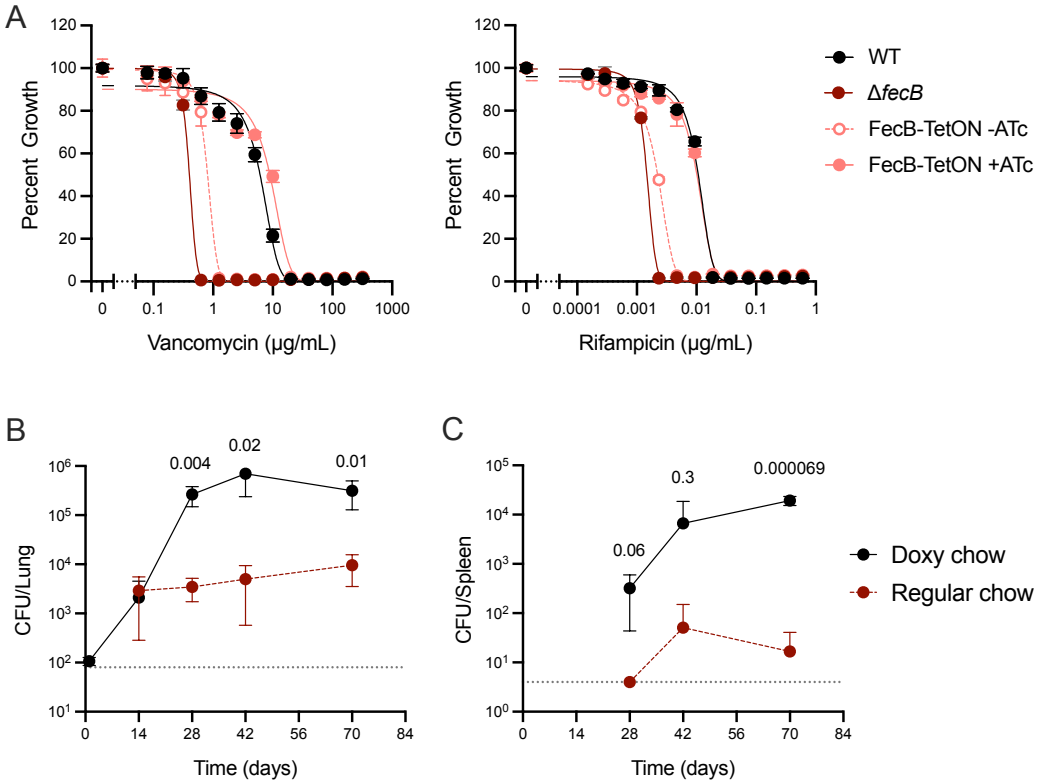

Figure 7. FecB is required for Mtb virulence. (A) MIC assays for vancomycin and rifampicin, in the absence or presence of ATc to induce *fecB* expression in the FecB-TetON strain (day 14). Percent growth calculated from no drug control wells. (B-C) Growth and persistence of FecB-TetON in the (B) lungs and (C) spleens of mice receiving doxy or regular chow. Data are average CFU counts from four mice per time point. Dashed black lines represent lower limit of detection. Statistical significance was determined by unpaired T-tests for each time point, p-value is shown above each pair analyzed. Error bars: ±SD. N independent experiments = 1 performed with triplicate cultures (A), 1 (B-C).